UNIVERSITY OF CALIFORNIA

Los Angeles

Nonlinear Behavior of Electron Plasma Waves Driven by Stimulated Raman Backscattering

A dissertation submitted in partial satisfaction of the

requirements for the degree of

Doctor of Philosophy in Physics

By

Donald Phillip Umstadter

1987

The dissertation of Donald Phillip Umstadter is approved.

Francis F. Chen

Francis Chen

Charles J. Buchanan

Charles Buchanan

Chan Joshi

Chan Joshi
Committee Co–Chair

John M. Dawson

John Dawson
Committee Co–Chair

University of California, Los Angeles

1987

Dedication

To Ed Flynn, my grandfather,

the remembrance of whom serves as an enduring source of inspiration.

Contents

List of Figures

Acknowledgments

There are many people I would like to thank for their support and assistance.

Of course, Chan Joshi, the principal investigator for the experimental program, who made this thesis possible and has done much to guide its progress.

Chris Clayton, who taught me everything I ever needed to know about ruby Thomson scattering.

Chris Darrow and Ron Williams, who put up with me for extended runs into the wee hours of the night.

Warren Mori for carrying out the simulations.

Frank Chen for providing the forum in which to exchange some of the useful ideas that I was given by himself and some of the others in the group, including: John Dawson, Tom Katsouleas and Humberto Figueroa, to name just a few.

Jim Gillis, for adopting the LaTeXstyle, which was used to typeset this thesis, to the UCLA thesis requirements.

Finally, I relied on my immediate family and friends for the support to keep plugging away at it for all these years.

Chapters 2 and 3 appeared in another form in D. Umstadter, et al. [1].

Chapter 4 will be been submitted for publication.

VITA

October 7, 1954	Born, New York, N. Y.
1978 - 1982	Research Engineer, Electrical Engineering Dept., University of California, Los Angeles.
1981	B.S., Physics, University of California, Los Angeles.
1983	M.S., Physics, University of California, Los Angeles.
1983	Teaching Assistant, Physics Dept., University of California, Los Angeles.
1984 - 1987	Post-graduate Research Engineer, Electrical Engineering Dept., University of California, Los Angeles.

PUBLICATIONS

W.A. Peebles, D. Umstadter, D.L. Brower, N.C. Luhmann, Jr.
'A Unidirectional Far Infrared Ring Laser'
Appl. Phys. Lett., **38**, 851 (1981).

C.E. Clayton, C. Joshi, C. Darrow and D. Umstadter
'Relativistic Plasma Wave Excitation by Collinear Optical Mixing'
Phys. Rev. Lett., **54**, 2343 (1985).

C.E. Clayton, C. Joshi, C. Darrow and D. Umstadter
'Relativistic Plasma Wave Excitation by Collinear Optical Mixing–Clayton et al. Respond'
Phys. Rev. Lett., **55**, 1652 (1985).

T. Katsouleas, C. Joshi, J.M. Dawson, F.F. Chen, C.E. Clayton, W.B. Mori, C. Darrow and D. Umstadter
'Plasma Accelerators'
Laser Acceleration of Particles (UCLA, 1985). C. Joshi and T. Katsouleas, Eds. (AIP Conf. Proc., New York, 1985).

C. Joshi, C. E. Clayton, C. Darrow and D. Umstadter
'Experiments on the Plasma Beat Wave Accelerator at UCLA'
Proceedings of the International Conference on Lasers '84, ed by K. M. Corcoran, D. M. Sullivan and W. C. Stwalley, pp. 467-472 (1985).

C. Clayton, C. Joshi, C. Darrow, D. Umstadter, and F.F. Chen
'Experimental Study of the Plasma Beat Wave Accelerator'
IEEE, Trans. on Nucl. Sci., **NS-32** (1985).

C. Darrow, D. Umstadter, C. Clayton and C. Joshi
'Controlled Studies of Wave-Wave Interactions in a Beat-Wave Laser Driven Plasma'
Laser Interaction and Related Plasma Phenomenon, H. Hora and G. Miley, Eds., Plenum Press (1986).

C. Darrow, D. Umstadter, T. Katsouleas, W. Mori, C. Clayton and C. Joshi
'Saturation of Beat Excited Plasma Waves by Electrostatic Mode Coupling'
Phys. Rev. Lett., **56**, 2629 (1986).

C. Darrow, W. B. Mori, T. Katsouleas, C. Joshi, D. Umstadter, and C. Clayton
'Electrostatic Mode Coupling of Beat Excited Electron Plasma Waves'
IEEE Trans. on Plasma Science, special Issue on Plasma-Based High Energy Accelerators, ed. by T. Katsouleas, **PS-15**, 107 (1987).

D. Umstadter, R. Williams, C. Clayton, and C. Joshi
'Observation of Wave Steepening in Electron Plasma Waves Driven by Stimulated Raman Scattering'
Phys. Rev. Lett., **59**, 292 (1987).

ABSTRACT OF THE DISSERTATION

Nonlinear Behavior of Electron Plasma Waves Driven by Stimulated Raman Backscattering

by

Donald Phillip Umstadter

Doctor of Philosophy in Physics

University of California, Los Angeles, 1987

Professor John M. Dawson, Co–Chair

Professor Chan Joshi, Co–Chair

The decay products of an incident light wave undergoing CO_2-laser–induced stimulated Raman and Brillouin scattering have been detected, the backscattered daughter light waves with use of an image dissector, and, simultaneously, the copropagting electron and ion plasma waves, with use of frequency- and wavenumber–resolved ruby Thomson scattering. Harmonic components of the steepened electron wave's electron density perturbation were also observed using ruby Thomson scattering. Measurements of the relative amplitudes of the electron

plasma wave harmonics agreed with predictions of nonlinear warm-plasma wave-steepening theory up to the maximum inferred amplitude of the fundamental component, $\tilde{n}_1/n_0 \leq 16\%$.

In addition to the expected Stokes satellite, a symmetrically shifted Anti-Stokes satellite was seen in the spectrum of the backscattered light. Also, in addition to the expected copropagating electron plasma wave, a counterpropagating electron wave was observed with use of ruby Thomson scattering. A computer simulation of the experiment not only corroborates these features of the backscattered spectrum but indicates that a further cascading to lower frequencies also occurs. These latter results may be explained by CO_2 and ruby laser Thomson scattering from counterpropagating electron plasma waves that originated from mode coupling of the SBS-induced ion wave with the SRS-induced electron wave.

Both nonlinear processes, steepening and mode coupling, may reduce the growth rate of the Raman backscattering instability.

Chapter 1

Introduction

A basic prediction of the nonlinear plasma wave theory of J. Dawson [2] is that as an electron plasma wave grows, its waveform steepens. E. Jackson [3] calculated the equivalent increase in the amplitudes of the harmonic components of the density perturbation relative to the fundamental. Thermal effects are included in a kinetic treatment by L. Kuz'menkov, et al. [6]. This process has several implications beyond its relevance to basic plasma physics [2] - [6]. It may, for instance, allow the plasma wakefield accelerator to exceed the linear transformer ratio [7]. The presence of the second harmonic, also, strongly affects the time evolution of the fundamental in numerical investigations of a beam-plasma system [8]. Steepening may also reduce Raman backscatter (SRS), a parametric instability that is of current interest in laser fusion because it may hinder the absorption of laser energy by the plasma [9]. An electrostatic plasma oscillation is excited in SRS by the ponderomotive force due to the beating between an incident electromagnetic wave (ω_0, k_0) with a light wave that is reflected in the backward direction from

plasma noise. By reflecting light more strongly, it further enhances the ponderomotive force and both it and the reflected wave grow exponentially. Unless it saturates or its pump becomes depleted, the plasma wave eventually breaks [2]. This is thought to be the origin of hot electrons that may preheat the fuel in laser fusion and thereby reduce compression efficiency [10]. The steepening of plasma waves driven by SRS is treated theoretically by P. Koch and J. Albritton [5].

Ion acoustic waves may be driven in an analogous process called stimulated Brillouin scattering (SBS). They may also steepen and result in harmonics. he harmonics of ion waves driven by SBS are observed by C. Walsh, et al. and by C. Clayton, et al. [11]

By modifying the electron plasma wave dispersion relation, the SBS-induced ion wave (ω_i, k_i) may couple to the the SRS-induced electron wave (ω_p, k_p)—if it occurs simultaneously—to excite other electron waves $[(\omega_p, k_p \pm mk_i)$, where m is an integer]. In an underdense plasma $(\omega_p/\omega_0 \ll 1)$, the ion wave and the electron wave have approximately equal wave numbers, $k_i \simeq k_p \simeq 2k_0$. The $m = -1$ mode thus has a high phase velocity, $v_\phi = c$. The $m = -2$ mode has almost the same phase velocity as the electron wave that would be excited by SRS without an ion ripple, but propagates in the opposite direction. The incident pump light wave may generate a new light wave that is Doppler-up–shifted by ω_p by coupling to the $m = -2$ mode. The SRS backscattered light wave $(\omega_0 - \omega_p)$ may cascade to lower frequency $(\omega_0 - 2\omega_p)$ by coupling to the $m = -1$ mode.

Plasma wave mode coupling is of considerable current interest because of its effects on laser fusion and plasma accelerator schemes [12] [13] [14] [15]. It is observed by C. Darrow, et al. [16] in experiments involving electron plasma waves driven by optical mixing and ion waves driven by SBS. Several other authors have

discussed mode coupling in the context of simultaneous SRS and SBS. Spatial harmonics of electron plasma waves driven by SRS and ion waves driven by SBS are observed by D. Villeneuve, et al. [17], but their origin could not be determined. Barr and Chen [12] have predicted the amplitudes of these coupled modes and calculated the amount that the SRS growth rate is reduced by the presence of the ion ripple. Aldrich et al. [14] have discussed the collapse of plasma wave, triggered by the coupling to ion waves. Figueroa and Joshi [13] have suggested that the characteristic double peak of the half-harmonic radiation could be due to SRS occuring in the presence of SBS near the quarter-critical layer.

Cascading is of current interest because it may limit the efficiency of the beat wave accelerator [18] [19]. It has been observed in experiments on optical mixing [20] but not in laser plasma experiments with a single pump.

Acting as decay mechanisms for the SRS induced electron plasma wave, these nonlinearities, steepening and mode coupling may reduce the growth rate of SRS.

We report the direct experimental observation of the decay products of CO_2-laser–induced SRS. Using an image dissector, we have observed the backscattered daughter light wave, and, using frequency and wave number resolved ruby Thomson scattering, we have simultaneously detected the daughter electron plasma wave. Also using ruby Thomson scattering, we have observed the steepening of electron plasma waves. In particular, we show that the amplitudes of the first three harmonics were consistent with the nonlinear theory of warm-plasma–wave growth [6]. Steepening is observed in electron plasma waves driven in discharge tube plasmas [21], but not in those driven by SRS.

We also report the observation of the usual decay products of SBS, the backscattered light wave and the ion wave, including its harmonics. Using ruby Thomson

scattering, we have detected a counterpropagating electron plasma wave with the same phase velocity as the copropagating electron plasma wave. In addition to the usual satellite that is red shifted by the plasma wave frequency, we have observed a symmetrically blue shifted satellite in the backscattered spectrum. A computer simulation not only confirms this result but reveals a cascading of light towards lower frequency. All of these spectral features may be explained by Thomson scattering from both high and low phase velocity, counterpropagating electron plasma waves, which originated from quasi-resonant mode coupling of an SBS induced ion wave with an SRS induced electron wave. The red shifted line in the ruby spectrum and the blue shifted shifted satellite in the backscattered spectrum are the result of Thomson scattering from the low phase velocity wave. The second Stokes satellite is the result of the SRS reflected light coupling to the fast wave and further cascading to lower frequencies.

The theory is reviewed in Chapter 2 of the thesis. We begin with a discussion of SRS followed by the theory of nonlinear plasma waves both in cold and in warm plasmas. The experimental arrangement and results are described in Chapter 3. This includes scattering spectra from the harmonics along with a comparison between the experimental results and the theory. The results of mode-coupling theory, experiments and simulations are discussed in Chapter 4. The effects of these nonlinearities on the growth of SRS and a summary of our results are presented in Chapter 5. A description of the CO_2 laser system is given in Appendix A.

Chapter 2

Wave Steepening Theory

The mechanism used in this experiment to drive the nonlinear plasma oscillations, stimulated Raman scattering, is discussed in Section 2.1 of this chapter.

The amplitudes of the harmonic components of the steepened density perturbation may be obtained in several ways. Three different approaches are shown in this chapter. The first two, Section 2.2.1 and Section 2.2.2, use the cold plasma approximation. The former was chronologically first. By starting very generally, it also gives the greatest physical insight. Traveling waves are treated as a special case. The latter was chronologically second and shows explicitly how the same results are obtained by assuming from the start the specific case of SRS. It also uses a more conventional expansion technique. Finally, in Section 2.3, a kinetic treatment is outlined, which both agrees with the results of Sections 2.2.1 and 2.2.2 in the cold plasma limit and gives thermal corrections to them as well.

2.1 Stimulated Raman Backcattering

Electron-plasma waves may be efficiently driven to large amplitudes with use of stimulated Raman backscattering (SRS). This is the parametric decay of a light wave into a backscattered, transverse, electromagnetic wave, and a collinear, longitudinal, electrostatic electron plasma wave. In a cold plasma, the three waves, the incident (ω_0, k_0), reflected (ω_1, k_1) and plasma (ω_2, k_2) waves, must obey their dispersion relations,

$$\omega_2 = \omega_p, \qquad {\omega_{0,1}}^2 = {\omega_p}^2 + c^2 {k_{0,1}}^2 \tag{1}$$

and the phase-matching conditions,

$$\omega_0 = \omega_1 + \omega_2, \qquad \mathbf{k}_0 = \mathbf{k}_1 + \mathbf{k}_2. \tag{2}$$

Because of the phase-matching conditions, in order for Raman backscatter to occur, the critical density, n_c, must satisfy $n/n_c \leq 0.25$. In an underdense plasma $(n/n_c \equiv {\omega_p}^2/{\omega_0}^2 \ll 1)$, the plasma-wave fundamental must have wave number, $k_2 \simeq 2k_0$.

The instability occurs only when the intensity of the incident pump exceeds a certain threshold value that is determined by balancing the growth rate with the damping rate. The threshold depends on several factors [22]: the density profile, with the lowest threshold corresponding to a homogeneous profile, filamentation effects that may locally raise the intensity of the pump, and ion wave induced density fluctuations. As the plasma wave grows, its waveform distorts in a process called wave steepening. Growth continues until one of three things happen: the pump becomes depleted, the plasma wave breaks, or the growth saturates. The latter may occur for many reasons, including: increased damping due to trapping

of background electrons, nonlinear effects, such as detuning of the frequencies of the either the pump or the plasma wave or further parametric decay of either the daughter electromagnetic or electrostatic wave.

Ion acoustic waves may be excited by the stimulated Brillouin scattering (SBS) instability, which for our experimental parameters has a lower threshold than SRS. Since the ion-acoustic frequency, $\omega_i \equiv k_i c_s \ll \omega_0$, where $c_s = (\gamma Z k_B T_e/m_i)^{1/2}$ is the acoustic velocity, the wave number of the ion-wave fundamental, k_i, also equals $2k_0$.

2.2 Cold Plasma Theory

In this section the cold plasma approximation is assumed. This means that the directed velocities of the electrons are assumed to be much greater than their thermal velocities.

2.2.1 Wave Steepening in General

As an electron-plasma wave grows, its waveform distorts because electrons at the top of the wave have greater velocities than those at the bottom. This process, called steepening was first predicted by Dawson [2] using a Lagrangian analysis. The amplitudes of the harmonic components of the density perturbation were first found in Eulerian coordinates by Jackson [3].

Here we briefly review their results. The model used was that of plane oscillations. The electrons oscillate in the x direction. The electrons in the $y-z$ plane oscillate similarly. Let the position of the sheet be described by the coordinate,

$$x = x_0 + D(x_0, t), \tag{3}$$

where x_0 is its equilibrium position and $D(x_0, t)$ is its displacement. Since the variation is in only one direction, the problem is basically one dimensional and Gauss' law may be used to obtain the electric field,

$$E(x,t) = 4\pi n_0 e D(x_0, t), \tag{4}$$

where n_0 is the background density. Eq. 4 holds provided that there is no sheet crossing, or if

$$\partial D(x_0, t)/\partial x_0 \geq -1. \tag{5}$$

The equation of motion is then simple harmonic

$$D(x_0, t) = a(x_0) \cos \omega_p t + b(x_0) \sin \omega_p t$$

In order to illustrate steepening Dawson examined the special case when $a(x_0) = 0$, $b(x_0) = C \sin kx_0$. At $t = 0$, one then has the following relations:

$$D = C \sin kx_0, \tag{6}$$

$$E = 4\pi e n_0 C \sin kx_0, \tag{7}$$

$$x = x_0 + D = x_0 + C \sin kx_0. \tag{8}$$

One may find E, normalized to its maximum amplitude, as a function of x by eliminating x_0 between Eq. 6 and 7. When this is done, the curves shown in Fig. 1 are obtained [2]. As C increases the waveform distorts until the point $C = 1/k$, beyond which the curves becomes multivalued. Since the curves must remain single valued, the point $C = 1/k$, which corresponds to the equality in Eq. 5, represents wavebreaking. Physically, the ordering of the electrons is no longer maintained.

We are interested in the density perturbation in Eulerian coordinates since that is what is measured in the lab. Conservation of the sheet and no sheet crossing

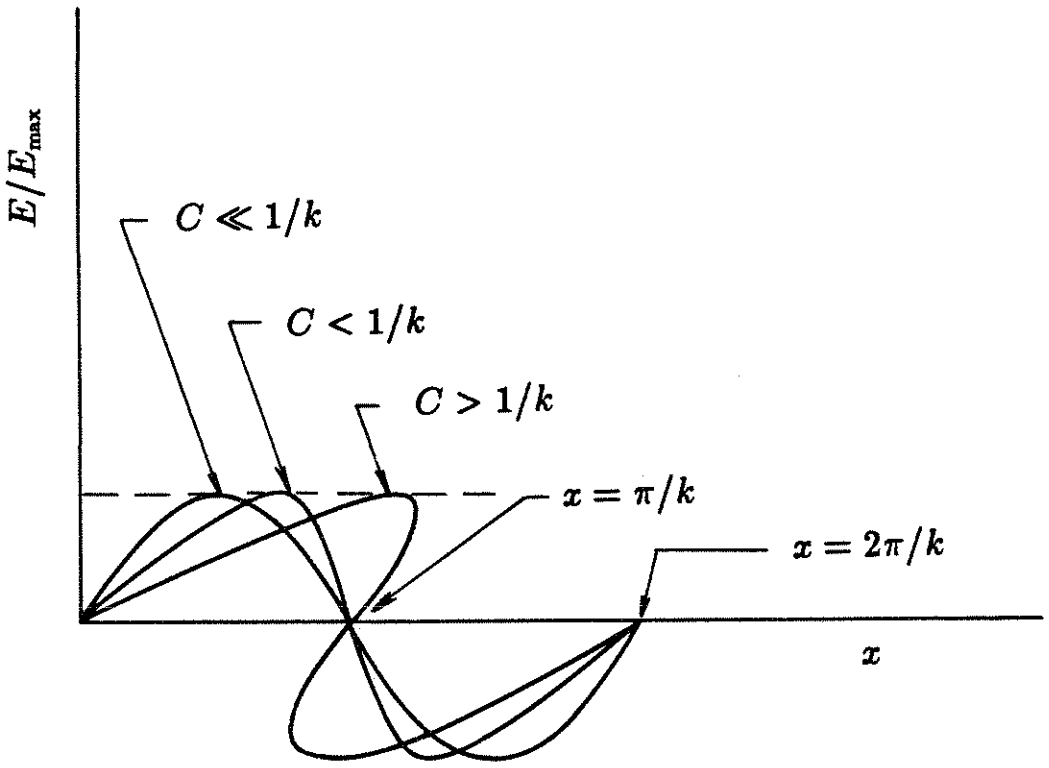

Figure 1: E as a function of x for various values of C.

leads to

$$n_0 dx_0 = n(x_0,t)dx$$

$$\Longrightarrow n(x,t) = n_0/[1+\partial D(x_0,t)/\partial x_0]$$

To obtain the explicit dependence of n(x,t) on the Eulerian variable x, Jackson [3] returned to Eqs. 3 and 4, applied an implicit function theorem due to Lagrange and used Poisson's equation to obtain

$$n(x,t) = n_0 \sum_{n=0}^{\infty} \frac{(-1)^n}{n!} \frac{\partial^n}{\partial x^n}[D(x,t)]^n. \tag{9}$$

We are concerned in this experiment with traveling waves, for which one assumes

$$D(x,t) = A(x,t)\cos(kx_0 - \omega_p t). \tag{10}$$

Then, plugging Eq. 10 into Eq. 9, one gets

$$\begin{aligned} n/n_0 \;\simeq\; & 1 + \\ & A(x,t)\sin(kx_0-\omega_p t) - \\ & A(x,t)^2\sin[2(kx_0-\omega_p t)] - \\ & 1.1A(x,t)^3\sin[3(kx_0-\omega_p t)] + \\ & .... \end{aligned}$$

Therefore,

$$\tilde{n}_m/n_0 = \alpha_m(\tilde{n}_1/n_0)^m, \tag{11}$$

where $\tilde{n}_m/n_0$ is the fluctuating density of the mth harmonic normalized to the background density. The coefficients for the first three harmonics are:

$$\alpha_1(\text{cold}) = \alpha_2(\text{cold}) = 1.0$$

$$\alpha_3(\text{cold}) = 1.1$$

We expect that for the mth harmonic $(\omega, k) = (m\omega_2, mk_2)$.

2.2.2 Wave Steepening in SRS

The coefficients of the harmonics of the density perturbation can be obtained in another way [5], which assumes from the onset that SRS is the driving mechanism. Here we rederive the coefficients for the case of SRS. It is found that they are the same as the ones found in Sec. 2.2.1.

The longitudinal force due to the electromagnetic waves is $(v \times B)_x$, where the propagation of the light wave is in the x direction. Using $v = eA/mc$, where v is the transverse electron velocity and A is the vector potential, the equation governing the cold plasma oscillations [23] can be written as

$$\ddot{\delta} + {\omega_p}^2\delta = -v\partial v/\partial x. \tag{12}$$

Here $\delta(x_0, t) = x - x_0$ is the displacement of a particle from its equilibrium position (x_0), $\omega_p = (4\pi Ne^2/m)^{1/2}$ is the plasma frequency, where N is the fixed background density, and the time derivative is Lagrangian (at constant x_0). The electromagnetic wave obeys [5]

$$(\partial^2/\partial t^2 + {\omega_p}^2 - c^2\partial^2/\partial x^2)v = {\omega_p}^2 v\partial\delta/\partial x \tag{13}$$

where the right hand side is the incremental electron current $-ev\Delta n_e$. The resonant part of the driver in Eq. 12 is proportional to $exp(i\lambda)$, where $\lambda = k_2x - \omega_p t = k_2x_0 - \omega_p t + k_2\delta$.

If we ignore dephasing terms which lead to relativistic effects, $k_2\delta$ has the form [23],

$$k_2\delta = D(t)cos[\lambda(x_0) + \phi(t)]. \tag{14}$$

The condition for wavebreaking [2], $|\partial\delta/\partial x_0 = 1|$ is equivalent to $D = 1$. The electron density, $n = N(1 - \partial\delta/\partial x)$, in the beat wave frame as it appears in Eulerian coordinates is periodic in λ but not sinusoidal; thus $\partial\delta/\partial x$ may be expanded in terms of all the harmonics of the beat wave [5].

$$\partial\delta/\partial x = \sum_{1}^{\infty} imF_m(t)\exp(im\lambda) + \text{c.c.} \tag{15}$$

The Fourier coefficients

$$F_m = (2\pi)^{-1}\oint d\lambda k\delta \times \exp(-im\lambda),$$

can be found from Eq. 14, Bessel's identity,

$$\exp(i\alpha\sin\theta) = \sum J_q(\alpha)\exp(iq\theta)$$

and the relation $d\lambda/d\lambda_0 = 1 + dk\delta/d\lambda_0$. The result is

$$F_m = (-i)^{m-1}m^{-1}J_m(mD)\exp(im\phi),$$

where F_m is the mth harmonic. We further expand the Bessel functions for small argument.

$$(mD \ll 1) \Longrightarrow J_m(mD) \simeq (mD)^m/2^m m!$$

The result is that one can express the amplitudes of the harmonics in terms of the fundamental as

$$\tilde{n}_m/n_0 = \alpha_m(\tilde{n}_1/n_0)^m, \tag{16}$$

where m is an integer ≥ 1,

$$\alpha_m(\text{cold}) = m^m/2^{(m-1)}m!, \tag{17}$$

and $\tilde{n}_m/n_0$ is the fluctuating density of the mth harmonic normalized to the background density. The coefficients, $\alpha_2(\text{cold}) = 1.0$ for the second harmonic and,

$\alpha_3(\text{cold}) = 1.1$ for the third harmonic are the same as those obtained in Section 2.2.1. The Bessel function expansion technique used to arrive at Eq. 16 is more familiar than the implicit function theorem technique used in Section 2.2.1. It also yields a series solution for all of the coefficients, Eq. 17. The physical contents of Sections 2.2.1 and 2.2.2, however, are equivalent.

2.3 Warm Plasma Theory

The plasma temperature in our experiment was finite. In this section, therefore, the cold plasma approximation is not assumed. This means that the thermal velocities of the electrons are on the order of, or greater than, their directed velocities.

We outline a treatment using the kinetic equations of a collisionless relativistic plasma [6], which, in the cold plasma limit, agrees with the fluid theory results of Sections 2.2.1 and 2.2.2, and gives thermal corrections to the coefficients, α_m. The relevant equations are:

$$\frac{\partial f_0}{\partial t} + c\frac{p_z}{p_0}\frac{\partial f_0}{\partial z} - eE\frac{\partial f_0}{\partial p_z} = 0; \tag{18}$$

$$\frac{\partial E}{\partial t} = -4\pi ec\int p_z f_0 \frac{d^3p}{p_0} = 0; \tag{19}$$

$$p_0 = (p^2 + m^2c^2)^{1/2}, \tag{20}$$

Wave solutions to these equations are considered corresponding to propagation along the z axis of an arbitrary waveform $E = E(\tilde{t})$, $f_0 = f_0(p, \tilde{t})$, while $\tilde{t} = t - qz/c$, $q = c/v_\phi$, and $v_\phi \ll$ c is the phase velocity of the wave. It is assumed for waves with velocities (v_ϕ) less than that of light that

$$\frac{\theta}{mc^2} = \frac{kT_e}{mc^2} \equiv \alpha \ll \frac{1}{\sqrt{1 - \frac{v_\phi^2}{c^2}}} - 1 \tag{21}$$

and that the number of captured particles is small.

The general solution of Eq. 18 can be written in the form

$$f_0 = f_0(p_x, p_y, \sigma(p, \tilde{t})), \tag{22}$$

where

$$\sigma(p,\tilde{t}) = p_z - \frac{c}{v_\phi}p_0 + \psi(\tilde{t}); \tag{23}$$

$$\psi(\tilde{t}) = \int eE(\tilde{t})d\tilde{t}. \tag{24}$$

The form of the function f_0 is taken to be a relativistic Maxwell distribution,

$$f_0 = A\exp\left(-\frac{c}{\theta}\tilde{p}_0\right), \tag{25}$$

where

$$\tilde{p}_0 = \frac{q\sigma + \left[\sigma^2 + (1-q^2)p_{0\perp}{}^2\right]^{1/2}}{1-q^2}, \tag{26}$$

and $p_{0\perp}{}^2 = p_0^2 - p_z^2$. The distribution function, Eq. 25, must be substituted in Eq. 19. However, we can expand in a series in the parameter, $\nu = eE_0/(\omega < p_0 >) \ll 1$. Therefore, Eq. 25 has the form

$$f_0(p,\tilde{t}) = \exp\left[\frac{\psi(\tilde{t})}{1-q\frac{v_z}{c}}\frac{\partial}{\partial p_z}\right] f_{0M}(p), \tag{27}$$

where $f_{0M}(p)$ is the relativistic Maxwell distribution [24]. Substituting Eq. 27 in Eq. 19, to the accuracy of terms of order ν^3, in order to determine the frequency correction of order ν^2, one obtains

$$\frac{1}{\omega_l^2}\frac{d^2\psi}{d\tilde{t}^2} + \psi = \frac{M\psi^2}{e} + \frac{N\psi^3}{e^2}, \tag{28}$$

where

$$M = -\frac{2\pi ce^3}{\omega_l^2}\int \frac{p_{0\perp}^2}{p_0^3\left(1-q\frac{v_z}{c}\right)^3}\frac{\partial f_{0M}}{\partial p_z}d^3p; \tag{29}$$

$$N = -\frac{2\pi ce^3}{\omega_l^2}\int \frac{p_{0\perp}^2\left(p_z - qp_0\right)}{p_0^5\left(1-q\frac{v_z}{c}\right)^5}\frac{\partial f_{0M}}{\partial p_z}d^3p, \tag{30}$$

and the dispersion relationship of linear theory was used, according to which the frequency of a linear wave, ω_l, having phase velocity, v_ϕ, equals

$$\omega_l^2 = 4\pi e^2\int \frac{\frac{c}{q}\frac{\partial f_{0M}}{\partial p_z}}{1-q\frac{v_z}{c}}d^3p. \tag{31}$$

In the range of prerelativistic temperatures and phase velocities that significantly exceed the thermal velocity ($kT_e/mv_\phi{}^2 \simeq 0.04 \ll 1$ and $(kT_e/m)^{1/2}/c \simeq 0.005 \ll 1$ in the present experiment),

$$\omega_l^2 = \omega_p{}^2 \left(1 + 3\frac{\theta}{mv_\phi^2}\right), \tag{32}$$

and in this region, the asymptotic values of M and N are

$$M \cong \frac{3}{2}\frac{e}{mv_\phi}\left(1 + 7\frac{\theta}{mv_\phi^2}\right), \tag{33}$$

$$N \cong \frac{1}{2}\left(\frac{e}{mc}\right)^2 - \frac{5}{2}\left(\frac{e}{mv_\phi}\right)^2\left(1 + 18\frac{\theta}{mv_\phi^2}\right). \tag{34}$$

It is evident from the asymptotic expressions found for M and N that $M\psi/e \sim \nu$, $N\psi^2/e^2 \sim \nu^2$. Therefore, the Krylov-Bogolyubov method [25] may be used to construct asymptotic solutions of Eq. 28. The following solutions are obtained.

$$\begin{aligned}\frac{d\psi}{d\tilde{t}} = E(\tilde{t}) \;=\; & E_0 \sin(\omega\tilde{t} + \phi_0) + \\ & \frac{ME_0^2}{3\omega}\sin\left[2(\omega\tilde{t} + \phi_0)\right] - \\ & \frac{3}{32}\left(N - \frac{2}{3}M^2\right)\frac{E_0^3}{\omega^2}\sin\left[3(\omega\tilde{t} + \phi_0)\right];\end{aligned} \tag{35}$$

$$\omega^2 = \omega_l^2\left[1 - \left(\frac{5}{6}M^2 + \frac{3}{4}N\right)\frac{E_0^2}{\omega_l^2}\right]. \tag{36}$$

The frequency of the fundamental is shifted relative to the frequency of a wave with infinitely small amplitude by an amount of order ν^2, while the coefficients M and N produce a contribution of the same order of magnitude. The result is that one can use Eq. 35 to write, as in Section 2.2.1, Eq. 11 or Section 2.2.2, Eq. 16, an expression for the amplitudes of the harmonics in terms of the fundamental,

$$\tilde{n}_m/n_0 = \alpha_m(\tilde{n}_1/n_0)^m, \tag{37}$$

where m is an integer ≥ 1 and $\tilde{n}_m/n_0$ is the fluctuating density of the mth harmonic normalized to the background density. For the conditions of our experiment ($T_e \simeq$ 10 eV and $v_\phi/c = 0.02$),

$$\alpha_1(\text{warm}) = 1.0,$$

$$\alpha_2(\text{warm}) = 1.3,$$

$$\alpha_3(\text{warm}) = 1.9.$$

If one sets $T_e = 0$, one retrieves the results of either Section 2.2.1 or 2.2.2.

Using Eqs. 33, 34 and 36, we find the nonlinear frequency shift in the nonrelativistic temperature limit:

$$\omega^2 = \omega_l^2 \left[1 - \frac{3}{8}\left(\frac{eE_0}{mc\omega_l}\right)^2 + \frac{15}{2}\left(\frac{eE_0}{mv_\phi\omega_l}\right)^2 \frac{\theta}{mv_\phi^2}\right]. \tag{38}$$

The correction to ω due to nonlinear effects from Eq. 38 is $\simeq 0.3\%$, less than the resolution of our spectrometer.

Since the nonlinear frequency shift was much less than ω_2, it is sufficient to assume for our purposes that the plasma wave has a frequency that equals the linear frequency, ω_l in Eq. 38 above. That is, the fundamental component obeys the linear warm plasma, or Bohm-Gross, dispersion relation, $\omega_2 = \omega_p(1+3(k_2\lambda_D)^2)^{1/2}$, where $\lambda_D = (k_B T_e/m_e{\omega_p}^2)^{1/2}$ is the Debye length. It will be shown in Sec. 3.2 how we measured ω_2, k_2 and $T_e \simeq 10$ eV and then used the dispersion relation to determine $n_0 \simeq 2.0 \times 10^{16}$ cm^{-3}. For these parameters, the thermal correction to ω_2 is small $\simeq 6\%$.

In a warm plasma, the wavebreaking limit is no longer given by $\tilde{E} = 1$ as in a cold plasma [2], but is instead [26]

$$\tilde{E} = \left(1 - \frac{1}{3}\beta - \frac{8}{3}\beta^{1/4} + 2\beta^{1/2}\right)^{1/2}, \tag{39}$$

where $\beta = 3{v_{th}}^2/{v_\phi}^2$. For our experimental parameters, $\beta = 0.12$ and we may write for the maximum density perturbation, $\tilde{n}_1/n_0 = \tilde{E}/\sqrt{4\pi m n_0 {v_\phi}^2} = 0.3$

Chapter 3

Wave Steepening Results

3.1 Experimental Arrangement

The plasma waves were excited in this experiment with a 10.6 μm, CO_2 laser (10 J, 2 ns), which was focussed by an $f/7.5$ lens to a spot of diameter, $d \leq 300$ μm onto an arc preionized H_2 plasma. A schematic diagram of the experimental arrangement is shown in Fig. 2. A description of the CO_2 laser system is given in Appendix A.

Raman backscattered light was diverted from the path of the incident CO_2 beam (pump) using a beamsplitter. Its amplitude could then be analyzed as a function of time with a resolution of 250 ps using a liquid-He–cooled detector in combination with a grating spectrometer, or as a function of frequency by adding an image dissector [27] (see Fig. 3). Whereas the grating spectrometer alone Fourier transforms frequency into space, when combined with an image dissector it Fourier transforms frequency into time. It does so by optically delaying higher-frequency bundles of rays by a greater amount of time than lower frequency

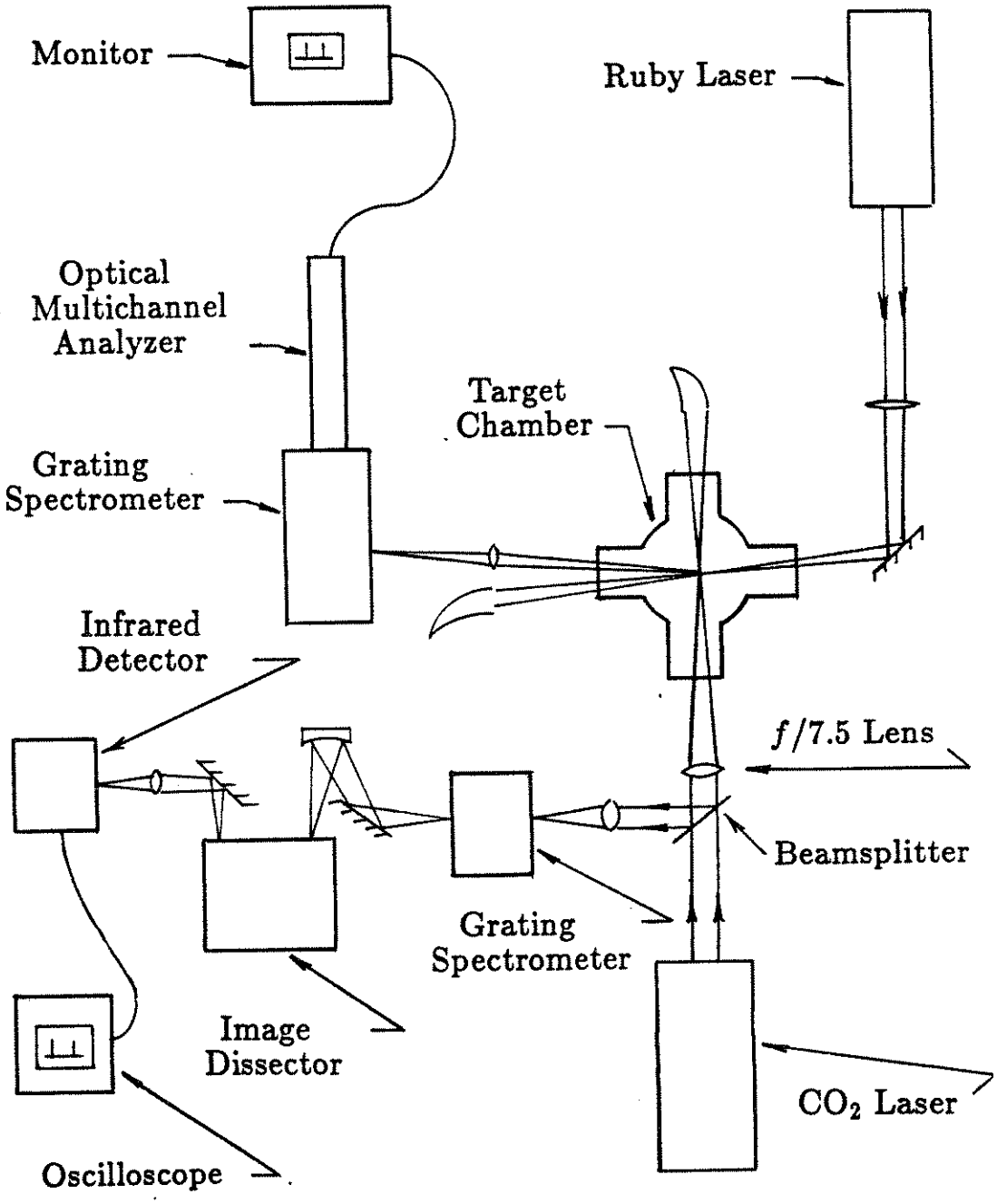

Figure 2: Schematic of the experimental arrangement.

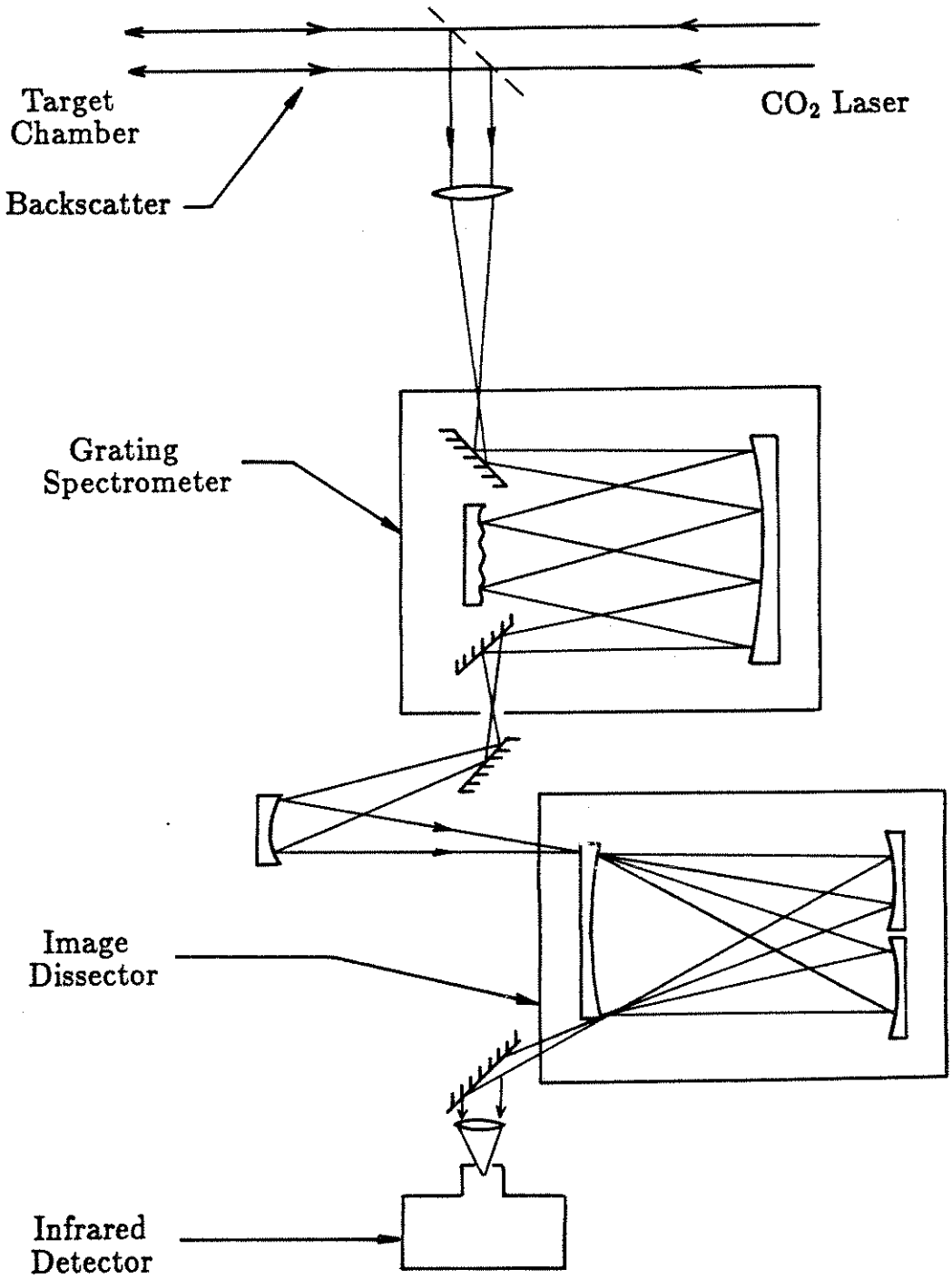

Figure 3: Schematic of the image dissector.

bundles. Each bundle of rays with a different frequency leaves the spectrometer at a different angle. After entering the image dissector, as shown in Fig. 3, each bundle will then be reflected by opposing mirrors—which are at a slight angle to the normal—a number of times depending on its frequency before walking off the face of one of the mirrors. If the bundles are then focused onto the detector and the pulse length is much less than the roundtrip time, then the output of the detector appears on an oscilloscope as discrete peaks in time, each corresponding to a different frequency bundle. In this way a single detector with a high sensitivity can replace an array of detectors with less sensitivity. The resolution of the image dissector was 0.07 μm. It was calibrated in both amplitude and frequency by running the CO_2 laser on two frequencies, 9.6 μm and 10.6 μm, and observing on an oscilloscope the time separation between the two peaks. This time separation is determined by the angle and distance between the mirrors.

The plasma waves were directly detected by Thomson scattering using a 1 J, 15 ns ruby laser pulse ($\lambda = .6943$ μm), which was synchronized in time with the CO_2 pulse and brought transversely to a focus at the location of the CO_2 beam waist. Since $v_{0,\,\mathrm{ruby}}/v_e \sim 0.03 \ll 1$, where $v_{0,\,\mathrm{ruby}} = eE/m\omega_{\mathrm{probe}}$ is the oscillating velocity of an electron in the field of the ruby probe beam and $v_e = (k_B T_e/m)^{1/2}$ is the thermal speed, the ruby laser acts as a nonperturbing probe [28]. The amplitude of the reimaged Thomson-scattered light was analyzed as a function of frequency by using an optical multichannel analyzer in tandem with a grating spectrometer. An optical multichannel analyzer is comprised of a linear array of 500 detectors. The spectrum is dispersed by the spectrometer across the detectors. The output of each detector is then read one at a time by a scanning electron beam and displayed on a monitor. The optical multichannel analyzer, calibrated by means of an Argon

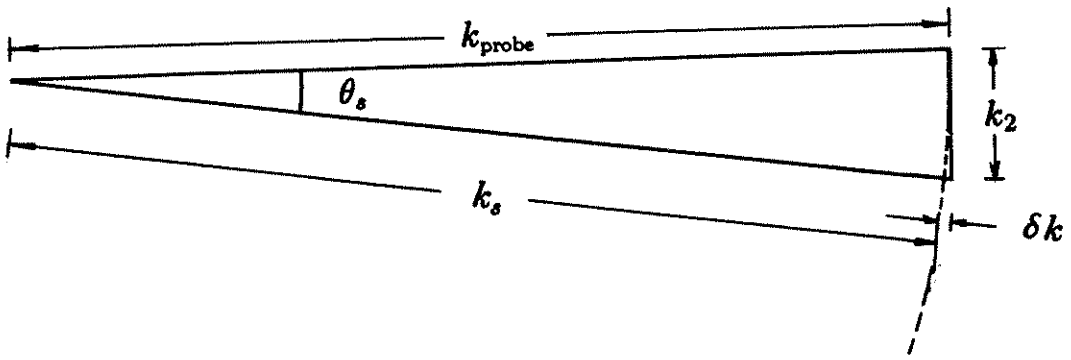

Figure 4: Ruby Thomson scattering geometry.

lamp with a known spectrum, had a resolution of $\simeq 1$ A°.

Similar to the case of SRS, the three waves in Thomson scattering, the ruby probe $(\omega_{probe}, k_{probe})$, the scattered light (ω_s, k_s) and the plasma wave (ω_2, k_2), must obey phase-matching conditions,

$$\omega_{probe} = \omega_s \pm \omega_2, \qquad \mathbf{k}_{probe} = \mathbf{k}_s \pm \mathbf{k}_2. \tag{40}$$

The frequency of the plasma wave was determined by the frequency shift, $\Delta\omega = \omega_2$, of either the SRS or the Thomson scatter. Its direction relative to the pump was determined by the sign of the frequency shift. Its wave number was determined by adjusting the scattering angle (θ_s) between the incident beam and the collection lens for the Thomson-scattered beam.

As shown geometrically in Fig. 4, the k-matching condition may be written in scalar form as

$$|k| = \left({k_s}^2 + {k_{probe}}^2 - 2k_{probe}k_s\cos\theta\right)^{1/2}. \tag{41}$$

When $\beta \equiv v/c \ll 1$, this reduces to

$$|k| \simeq 2|k_{probe}|\sin\theta/2. \tag{42}$$

Eq. 42 applies to the case of coherent scattering from a well defined wave ($k\lambda_D = k_2\lambda_D \leq 1$), excited by Raman backscatter in an underdense plasma, for which $k_2 \cong 2k_0$ and $n/n_{c,0} \ll 0.25$, because

$$\beta = \omega_2/k_2 c \cong (k_0/k_2)(\omega_2/\omega_0) \cong (1/2)(n/n_{c,0})^{1/2} \simeq 0.02 \ll 1,$$

where $n_{c,0}$ is the critical density for the pump radiation.

It should be noted that the triangle shown in Fig. 4 is not equilateral because the wave number of the scattered ruby light, k_s, is greater by ω_p/c than k_{probe}. If an equilateral triangle were used instead, the ruby would be probing a component of the plasma wave at an angle of 1° with respect to the direction of the CO_2 pump. This error becomes significant for the case of Thomson scattering from plasma waves with $\beta \sim 1$.

Eq. 42 may be used to write [28]

$$\alpha \equiv \frac{1}{k\lambda_D} = \frac{1.08 \times 10^{-4}\lambda_{\text{probe}}(\text{cm})}{\sin\theta/2}\left[\frac{n(\text{cm}^{-3})}{T_e(\text{eV})}\right]^{1/2}. \tag{43}$$

The parameter α distinguishes two scattering regimes. When $\alpha \geq 1$ or $\lambda \geq \lambda_D$, the incident probe wave interacts with the Debye shielded charges, resulting in coherent scattering. In the regime $\alpha \ll 1$ or $\lambda \ll \lambda_D$, the scattered spectrum no longer depends on the collective behavior of the charges, but instead on their random distribution; the result is incoherent scattering. From Eq. 43, we find that incoherent scattering ($\alpha \leq 0.1$) would not be possible for our experimental parameters ($T_e = 10$ eV and $n = 2 \times 10^{16}$ cm^{-3}) at any angle, even if we had the required probe power. It would be possible if the ratio n/T_e were less by a factor of ten or if we used a probe with wavelength, λ_{probe}, less by a factor of three. We do, however, expect coherent scattering ($\alpha = 5$) from the fundamental component of an SRS driven electron plasma wave, with $k_2 = 2k_0$, to occur at an angle, $\theta_s \simeq 7°$.

We also expect coherent scattering from the second harmonic, with $k_2 = 4k_0$, at $\theta_s \simeq 14°$ and from the third harmonic, with $k_2 = 6k_0$, at $\theta_s \simeq 21°$. Because of k-matching, both the probe beam and the collection lens must be changed when probing for the second and third harmonic components. If only the collection lens were changed or if a larger lens were used to collect light from all the components at once, the higher-harmonic components would not be matched.

3.2 Scattering Spectra

Two narrow frequency lines were observed when the collection lens for the ruby Thomson-scattered light was at $\theta_s = 7°$, the angle corresponding to $k_2 = 2k_0(1 \pm 15\%)$; the uncertainty was due to the 4.5° angle subtended by the collection lens. The peak on the right of Fig. 5(a), which shows a photograph of the optical multichannel analyzer output, is due to Thomson scattering from an SBS induced ion wave. SBS was expected because the pump laser intensity, I, was well above its threshold [29]. This feature was detected only when the CO_2 laser was incident on the plasma and thus was not due to ruby stray light from specular reflections. The Thomson-scattered signal from the ion wave appears unshifted in frequency because the ion-acoustic frequency, ω_i, as defined in Sec. 2.1, was less than the resolution of the spectrometer. The acoustic frequency was, nevertheless, measured by using a spectrometer with a greater resolution and in this way the electron temperature was determined to be $T_e \simeq 10$ eV. The peak on the right of Fig. 5(b), which shows an oscilloscope trace of the image-dissector output, is due to red shifted SRS backscatter, measured simultaneously with the 7° Thomson scattering [Fig. 5(a)]. The negative pulse on the left is a fiducial used to determine

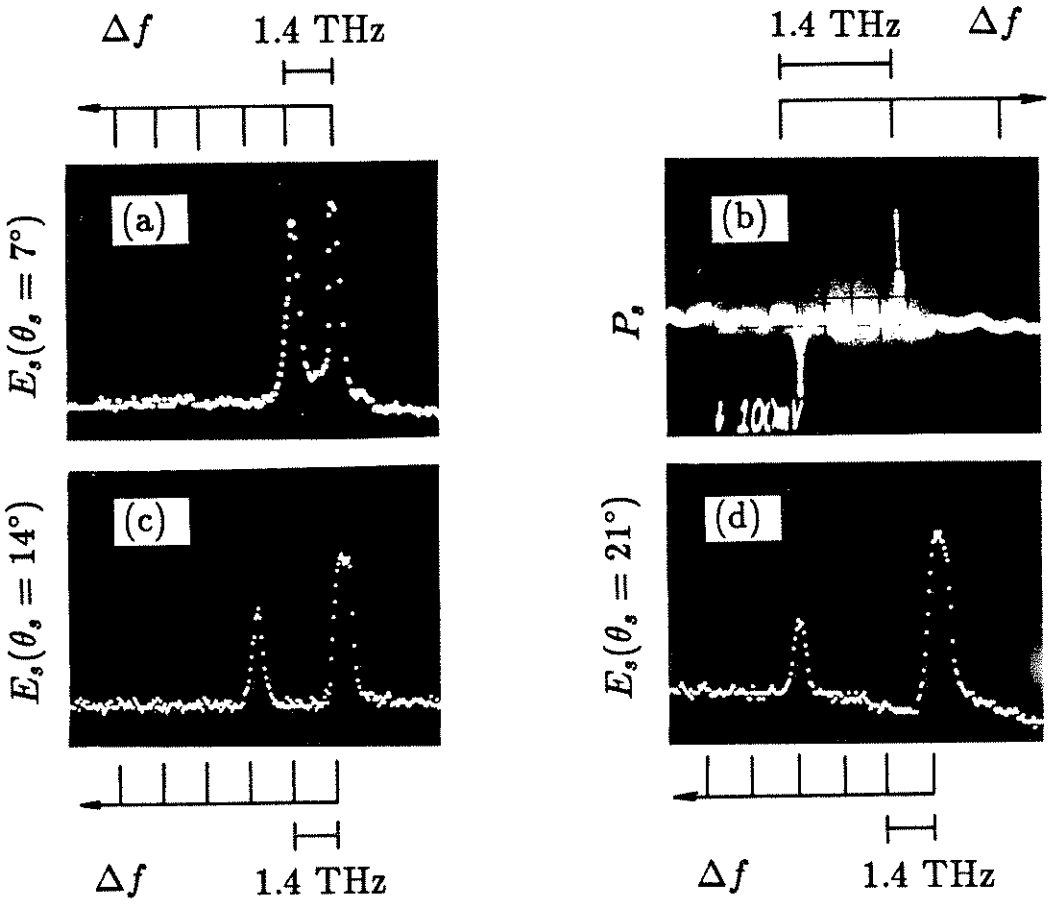

Figure 5: Frequency- and wave-number–spectra of the plasma wave harmonics. (a) Thomson-scattered light from the fundamental of the ion wave (right) and plasma wave (left). (b) Raman backscatter (right) and a fiducial at 10.6 μm (inverted, left). (c) The second and (d) third harmonics of the ion wave (right) and the plasma wave (left).

the frequency shift (Δf) of the backscattered light with respect to 10.6 μm, the incident pump wavelength. The peak on the left of Fig. 5(a) is due to Thomson-scattered light that is blue shifted in frequency (Δf) by an amount that, assuming $\Delta\omega = \omega_2$ and $T_e = 10$ eV, is consistent with a plasma density of 2.0×10^{16} cm^{-3} ($n_0/n_c = 2 \times 10^{-3}$) and a value $k_2\lambda_D = 0.2$. Again, no peak was observed when the probe was fired without the CO_2 laser. These results imply that this was not incoherent scattering from thermal fluctuations, but collective scattering ($\alpha \gg 1$) from the fundamental component of a plasma wave that was propagating in the direction of the pump with $(\omega, k) = (\omega_2, k_2)$.

By varying the arc fill pressure and the relative timing between the preionization and the laser pulse, the plasma density could be continuously adjusted. As shown in Fig. 6, the densities calculated from the frequency shifts of both the SRS and the 7° Thomson scattering agree over the density range of the experiment. We thus conclude that both were the decay products of the incident light wave; the backscatter was the daughter light wave and the Thomson scatter was scattering from the fundamental component of the daughter plasma wave.

We chose to operate at $n_0/n_c = 2 \times 10^{-3}$; it was the density at which SRS and thus the plasma-wave amplitude was maximum, possibly because of the competition between collisional damping, which is more important at higher n_0, and Landau damping, which dominates at lower n_0 [30].

The peak on the left in Fig. 5(c)—which is due to ruby probe light scattered at $\theta_s = 14°$, the angle corresponding to $k_2 = 4k_0(1 \pm 8\%)$—is shifted in frequency by $\Delta\omega = 2\omega_2$; that is twice the frequency shift of the probe light scattered at $\theta_s = 7°$ [Fig. 5(a)]. By monitoring the shift in frequency of the SRS backscattered light [Fig. 5(b), 6], it was found that the density and thus the plasma wave frequency,

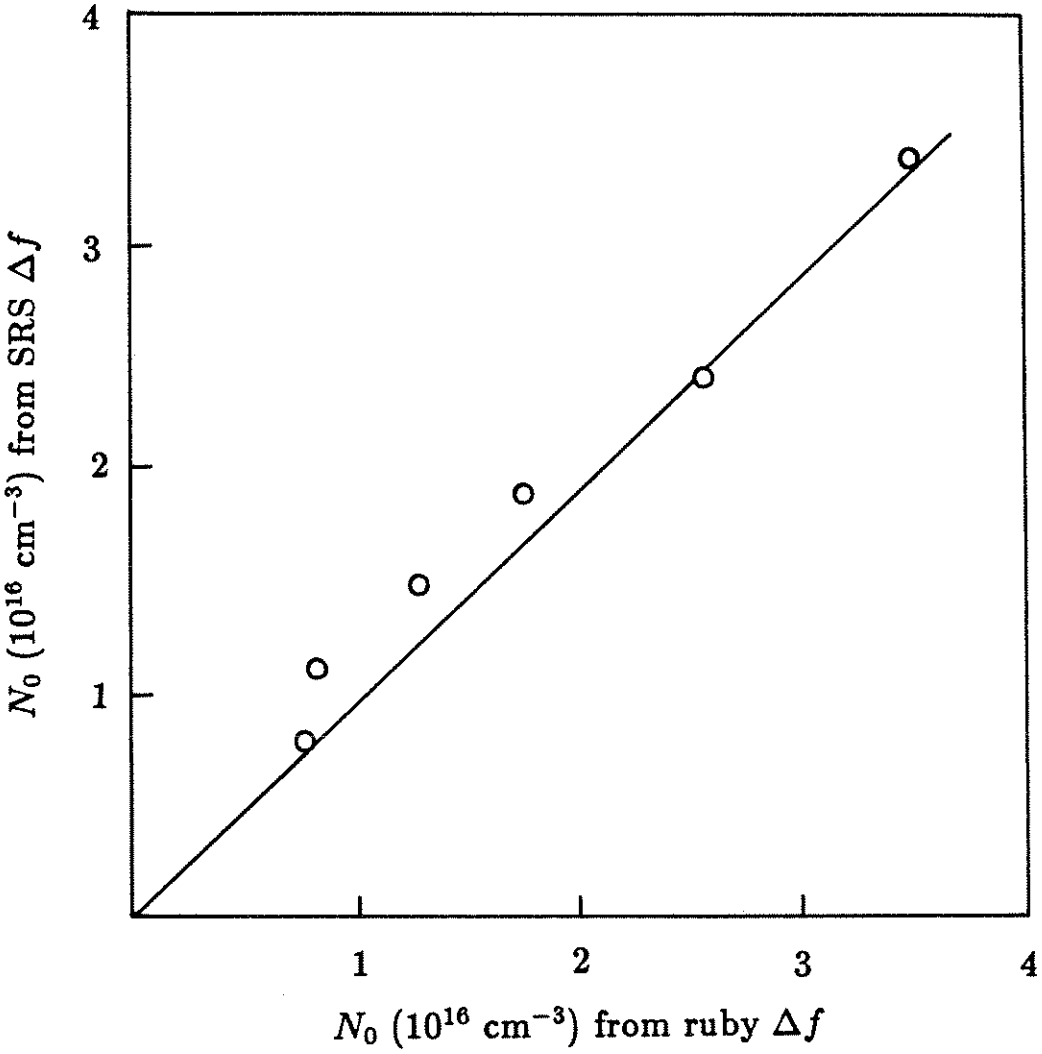

Figure 6: Density (N_0) inferred from the ruby Thomson scatter frequency shift, Δf, plotted with N_0 inferred from the SRS Δf.

ω_2, was the same for both $\theta_s = 7°$ and $\theta_s = 14°$ scattering. The peak on the left of Fig. 5(c), therefore, is due to scattering from the second harmonic component of the plasma wave with $(\omega, k) = (2\omega_2, 2k_2)$. The peak on the right of Fig. 5(c) is due to scattering from the second harmonic of the ion wave. Similarly, the two peaks in Fig. 5(d), corresponding to ruby light scattered at $\theta_s = 21°$, are attributed to the third harmonic component of the plasma wave, with $(\omega, k) = (3\omega_2, 3k_2)$, and the third harmonic of the ion wave.

Qualitatively, the same spectrum of modes would be expected if this were Raman-Nath scattering and not Thomson scattering from plasma wave harmonics. In the former process, light scattered from a traveling wave—such as an acoustic wave, as in their original paper [31], or a plasma wave, as in the present case—may be diffracted into several orders. Each of the orders is shifted by a multiple of the fundamental frequency. It is shown [32], however, that the ratio of the Raman-Nath–scattered power, diffracted into the first order, to the Thomson-scattered power from the fundamental is approximately 1%. The ratio for the second order (second harmonic) is $0(10^{-6})$. The spectrum we are observing therefore is due to Thomson scattering from the harmonic components of a plasma wave and not Raman-Nath scattering.

Although harmonics of electron plasma waves excited in a discharge tube are observed [21], the results of Fig. 5 are, we believe, the first observation of harmonics of plasma waves driven by SRS. The wave numbers and frequencies of the harmonics thus agree with the theory. It is still to be shown that their amplitudes do as well.

3.3 SRS Amplitude Time History

Time histories of the amplitudes of both the incident laser pulse and the SRS are shown in Fig. 7(a, b). In order to measure the incident pulse, part of the incident beam was diverted with use of a beamsplitter and then focussed onto the cold detector. Instead of using the image dissector as was done in Fig. 5(b), the backscatter time history was measured by first dispersing it in frequency with a grating and then focusing it onto the cold detector. A bandpass filter and saturable absorber gas cell were used to absorb the unshifted 10.6 μm light and pass only the 11.1 μm SRS. The oscilloscope traces were recorded with a fast, 1 GHz scope. The time resolution of the scope-detector combination was 250 ps. The risetime of the SRS, as can be seen in Fig. 7(b), was instrument limited. This is expected because of the small value for the estimated homogeneous growth rate of the SRS [4],

$$\gamma_0{}^{-1} = \left(\frac{kv_0}{2\sqrt{2}} \frac{\omega_p}{\sqrt{\omega_2(\omega_0 - \omega_2)}} \right)^{-1} = 28\omega_p{}^{-1} = 3.5\text{ps}.$$

The quantity $v_0 = eE_0/m\omega_0$ is the quiver velocity of an electron in the field of the laser and all the other quantities are as defined previously. After reaching a peak value, the SRS follows the incident CO_2 light pulseshape as it decays. A discussion of possible saturation mechanisms follows in Section B. Of course, the time histories in Fig. 7 average over oscillations in amplitude for time scales shorter than 250 ps.

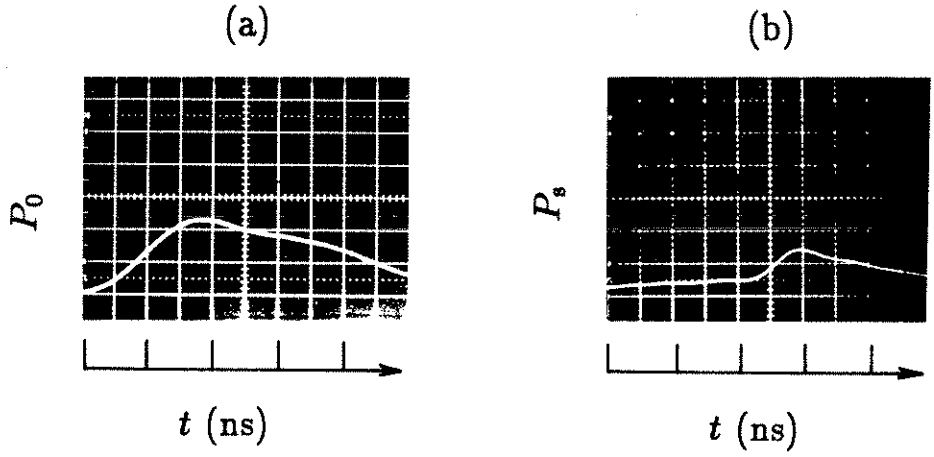

Figure 7: Time history of the incident (a) and backscattered (b) pulse.

3.4 Scattering Amplitude Correlation

In order to compare the experimentally measured amplitudes with the theory, it must first be shown that the amplitude of the light Thomson-scattered at $\theta_s = 7°$, due to the fundamental component of the plasma wave [Fig. 5(a)], is correlated with the amplitude of the backscattered light [Fig. 5(b)]. The ruby Thomson scattering diagnostic can then be used to measure the amplitude of the higher harmonic components at $\theta_s = 14°$ or $\theta_s = 21°$, while the SRS is used to simultaneously measure the amplitude of the fundamental.

The peak amplitudes of the backscattered power (P_s) are plotted in Fig. 8 with the simultaneously measured amplitudes of the 7° Thomson-scattered energy (E_s). The solid line is a best fit to the data and the dotted lines show the spread in measured values. The Bragg scattering formula [28],

$$\frac{E_s/\tau_p}{E_0/\tau_0} \simeq \frac{P_s}{P_0} = \frac{1}{4}\tilde{n}^2 {r_0}^2 {\lambda_{\text{probe}}}^2 d^2, \tag{44}$$

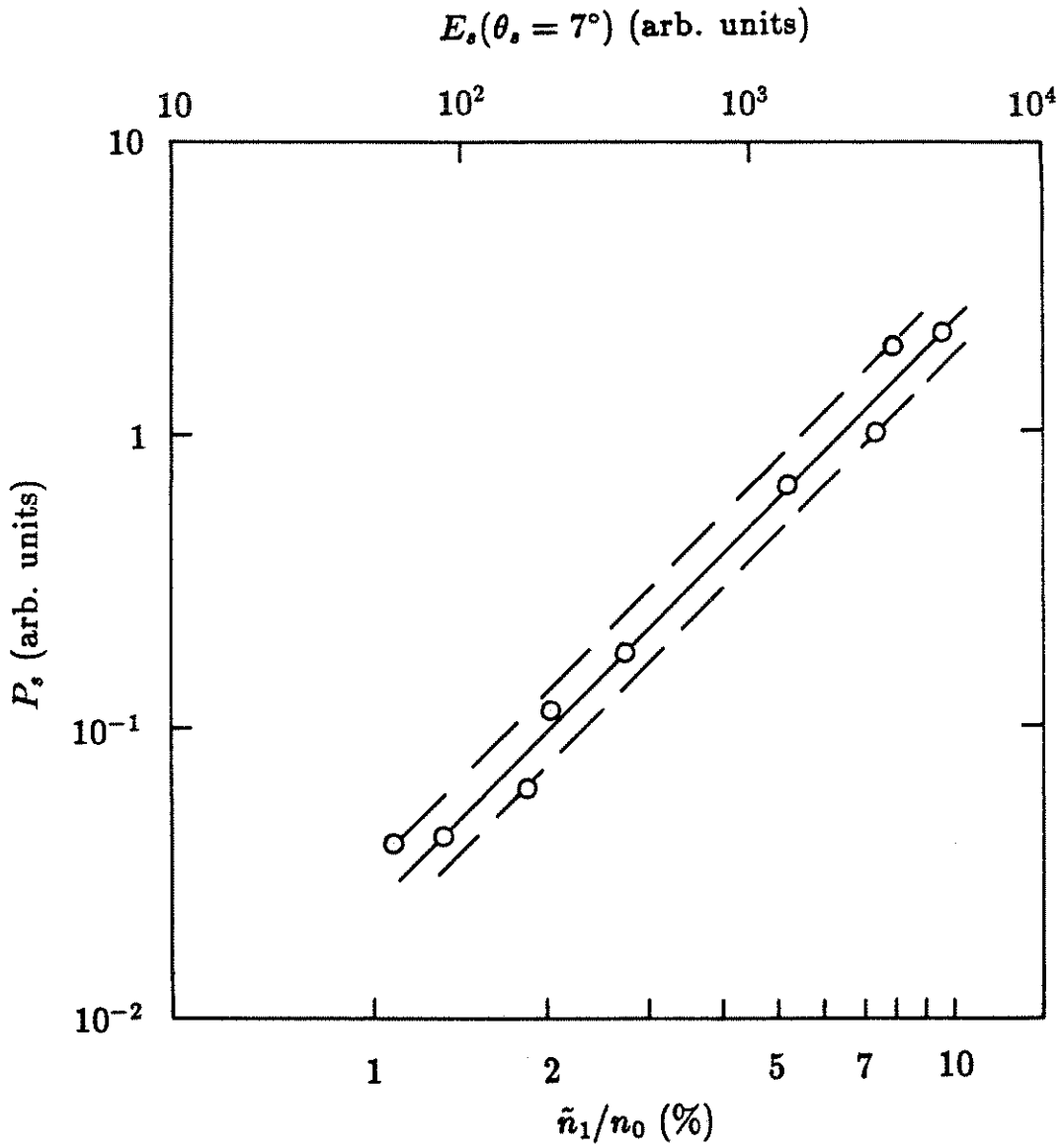

Figure 8: Amplitude correlation of the ruby Thomson scatter (E_s) with Raman backscatter (P_s).

where r_0 is the classical electron radius, allows conversion of $E_s(\theta_s = 7°)$ to $\tilde{n}_1/n_0$, assuming: an effective $d = 120$ μm [20], or approximately one half of the width of the CO_2 beam waist [20], and a ratio of the ruby pulse length to the lifetime of the plasma wave, $\tau_0/\tau_p \simeq 15$ ns/1.5 ns $= 10$ [see Fig. 7(b)]. The latter was determined from measured time histories of both the ruby pulse (τ_0) and the backscattered pulse (τ_p). The scattering system was calibrated absolutely by directly measuring the power of the incident probe beam, P_0, with the same optics and optical multichannel analyzer that was used to measure P_s.

The condition for ion wave harmonic generation is $(k_i\lambda_D)^2 \simeq (\tilde{n}_1/n_0)_{ion}$ [11]. From the amount of SBS and Eq. 44, $\tilde{n}_1/n_0$ for the ion wave was determined to be typically $(\tilde{n}_1/n_0)_{ion} = 10\%$. Since $(k_i\lambda_D)^2 = 4\%$, ion-wave harmonics were thus to be expected.

The correlation of Fig. 8 allows us to read off the value of $\tilde{n}_1/n_0$, measured by ruby Thomson scattering, from the amplitude of the backscatter (P_s). But before proceeding to compare the amplitudes of the harmonics, we first check that the value of the backscattered amplitude is consistent with the corresponding value of $\tilde{n}_1/n_0$. We do this by using a formula for the backscatter which is analogous to the Bragg formula for the Thomson scatter, Eq. 44.

As can be seen from Fig. 8, the maximum basckscatter corresponds to a value of $\tilde{n}_1/n_0 = 10\%$, measured by ($\theta_s = 7°$) ruby Thomson scattering. This is consistent with a range of $9\% \leq (\tilde{n}_1/n_0)_{SRS}$, which is inferred from the amount of backscatter and the formula for the reflectivity given by Kruer [34],

$$R = \tanh^2\left[\frac{\pi}{2}\frac{\tilde{n}_1}{n_0}\frac{n_0}{n_c}\frac{L}{\lambda_{pump}}\left(1 - \frac{n_0}{n_c}\right)^{-\frac{1}{2}}\right], \tag{45}$$

assuming a value for the interaction region of $L \leq 2$ mm.

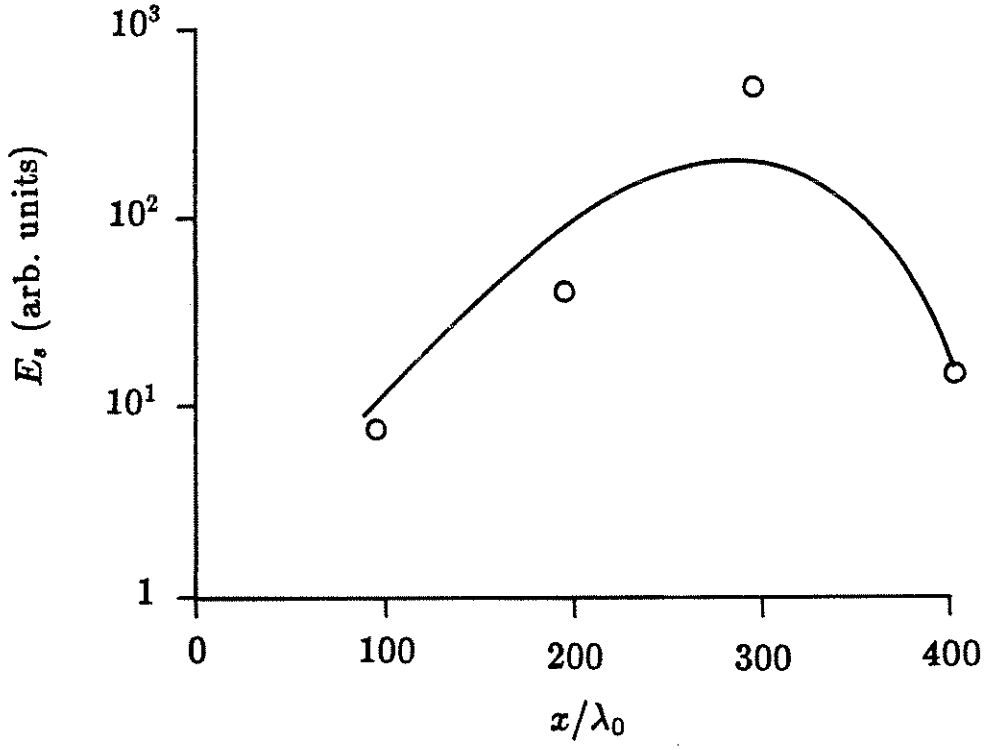

Figure 9: Plasma wave axial profile measured by ruby Thomson scattering.

The upper bound on the interaction region, $L \leq 2$ mm, was measured by observing the level of scattering while scanning the plasma wave with the ruby probe along the axis of the CO_2 laser focus and simultaneously monitoring the amplitude of the Raman backscatter [Fig. 9]. The edges of the interaction region were taken to be where there was no Thomson scattering on shots when SRS was detected. We would expect this to give an upper bound for L because the plasma wave can be located in different positions axially while remaining the same length from one shot to the next. L is the length of a region over which several interactions may occur. Since the backscatter used in Eq. 45 is integrated over all

of the interactions, it is correct to use this length in Eq. 45.

As can be seen by Eqs. 44 and 45, in the limit of small argument both SRS and Thomson scattering have the same dependence on $\tilde{n}_1/n_0$. The linear correlation of Fig. 8, therefore, indicates that not only the maximum value, but all values of $(\tilde{n}_1/n_0)_{\rm TS}$ are consistent with the inferred range of $(\tilde{n}_1/n_0)_{\rm SRS}$.

3.5 Scaling of the Harmonics

By virtue of the correlation of Fig. 8, while Thomson scattering is used to measure either $\tilde{n}_2/n_0$ or $\tilde{n}_3/n_0$—but not both on the same shot—SRS can be used to infer $\tilde{n}_1/n_0$. The amplitude of the backscattered light is plotted in Fig. 10 with the amplitude of the light Thomson scattered at $\theta_s = 14°$ and $\theta_s = 21°$ from the second and third harmonic, respectively. The scale of the ordinate in Fig. 10 was changed from $E_s(\theta_s = 14°)$ to $\tilde{n}_2/n_0$ using $d = 85$ μm and from $E_s(\theta_s = 21°)$ to $\tilde{n}_3/n_0$ using $d = 70$ μm as was done in Fig. 8. Here, assuming that the harmonics had Gaussian profiles and were related to each other by Eq. 37 above, we took d to be the width at which the amplitude was reduced by $1/e$ of its maximum value. The scale of the abscissa was determined by using the correlation that is represented by the solid line in Fig. 8 to infer $\tilde{n}_1/n_0$ from the SRS amplitude. The predictions of the warm-plasma theory, represented by the solid lines in Fig. 10, were obtained using Eq. 37 above, ie. $(\tilde{n}_2/n_0)_{\rm pred} = 1.3(\tilde{n}_1/n_0)^2$ and $(\tilde{n}_3/n_0)_{\rm pred} = 1.9(\tilde{n}_1/n_0)^3$. The uncertainties in $(\tilde{n}_2/n_0)_{\rm pred}$ and $(\tilde{n}_3/n_0)_{\rm pred}$, represented by the dotted lines in Fig. 10, were due to the uncertainty in $\tilde{n}_1/n_0$, represented by the dotted lines of Fig. 8. The data of Figs. 8 and 10 were obtained on separate data runs. There are values of P_s in Fig. 10 that are larger than its maximum value in Fig. 8,

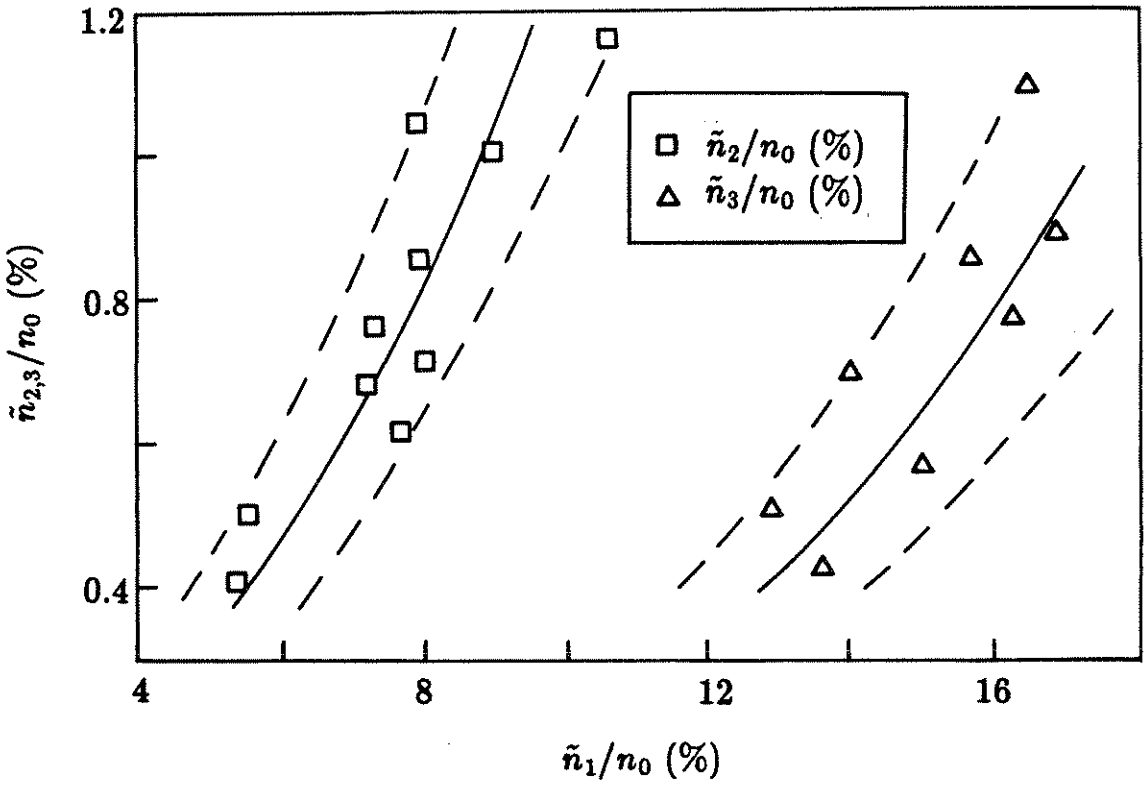

Figure 10: Amplitude of Thomson scatter from the second harmonic ($\tilde{n}_2/n_0$) and third harmonic ($\tilde{n}_3/n_0$) as a function of Raman backscatter ($\tilde{n}_1/n_0$).

$P_s(\tilde{n}_1/n_0 = 10\%)$. The curve of Fig. 8, therefore, had to be extrapolated to the range $10\% < \tilde{n}_1/n_0 \leq 16\%$. This was well justified not only because of the correlation at lower values, but because both Eqs. 44 and 45 depend only on $\tilde{n}_1/n_0$. As shown in Fig. 10, $\tilde{n}_2/n_0$ agrees with $(\tilde{n}_2/n_0)_{\text{pred}}$, and $\tilde{n}_3/n_0$ agrees with $(\tilde{n}_3/n_0)_{\text{pred}}$ for all values. Thus not only do the wave numbers and frequencies of the harmonics agree with theory, so do their amplitudes.

Chapter 4

Mode Coupling

It was expected from the wave-number–matching condition on the three waves in SRS, described in Sec. 2.1, that a plasma wave propagating in the direction of the incident light wave and a red shifted backscattered light wave would be detected. These waves were indeed detected as was shown in Figs. 5(a) and (b). As would be expected from the ruby Thomson scattering geometry (see Fig. 4), the ruby light scattered from the copropagating electron plasma wave was blue shifted in frequency. However, a symmetrically blue shifted satellite in the backscattered spectrum, shown in Fig. 13(a), and a red shifted satellite in the ($\theta = 7°$) ruby Thomson-scattered spectrum, shown in Fig. 15, were also detected.

As we will show, these spectral features may arise from Thomson scattering from high and low phase velocity, counterpropagating electron plasma waves, which may result from the coupling of the decay products of simultaneously occurring SRS and SBS.

4.1 Thomson Scattering from Coupled Modes

It has been both predicted [15] and shown experimentally [16] that, by modifying the electron plasma wave dispersion relation, a ripple produced by an ion wave may couple to an electron plasma wave and result in plasma wave spatial harmonics. The electron-plasma–wave spatial harmonics that result from mode coupling have wave numbers k $= k_p \pm mk_i$, where m is an integer [15]. In the present case, where the ion wave is driven by SBS ($k_i \simeq 2k_0$) and the electron wave is driven by SRS ($k_p = 2k_0 - \omega_p/c \equiv 2k_0 - \delta k$), the $m = -1$ coupling gives rise to a counterpropagating, high phase velocity, $v_\phi = c$, electron wave with $(\omega, k) = (\omega_p, k_p - k_i) \simeq (\omega_p, -\delta k)$. The k-matching diagram for this mode is shown in Fig. 11(c). Mode coupling is shown diagramatically in Fig. 12. The $m = -2$ coupling gives rise to a counterpropagating electron plasma wave $[(\omega, k) = (\omega_p, k_p - 2k_i) \simeq (\omega_p, -[2k_0 + \delta k])]$ that in an underdense plasma has almost the same phase velocity as the copropagating wave that would be driven by SRS without the ion ripple. The k-matching diagram for this mode is shown in Fig. 11(d). Although an infinite number of frequency eigenmodes with the same wave number are possible [13], only the modes with small values for m have significant growth rates [12]. The presence of the SBS induced density ripple, by generating these new modes, may reduce the growth rate of SRS [12]. Mode coupling is shown diagramatically in Fig. 12.

The incident CO_2 pump light wave ($k = k_0$) may Thomson scatter from the counterpropagating slow wave, the $k = -(2k_0 + \delta k)$ mode, and result in a backscattered light wave ($k = -[k_0 + \delta k]$) that is blue shifted by ω_p. The k-matching

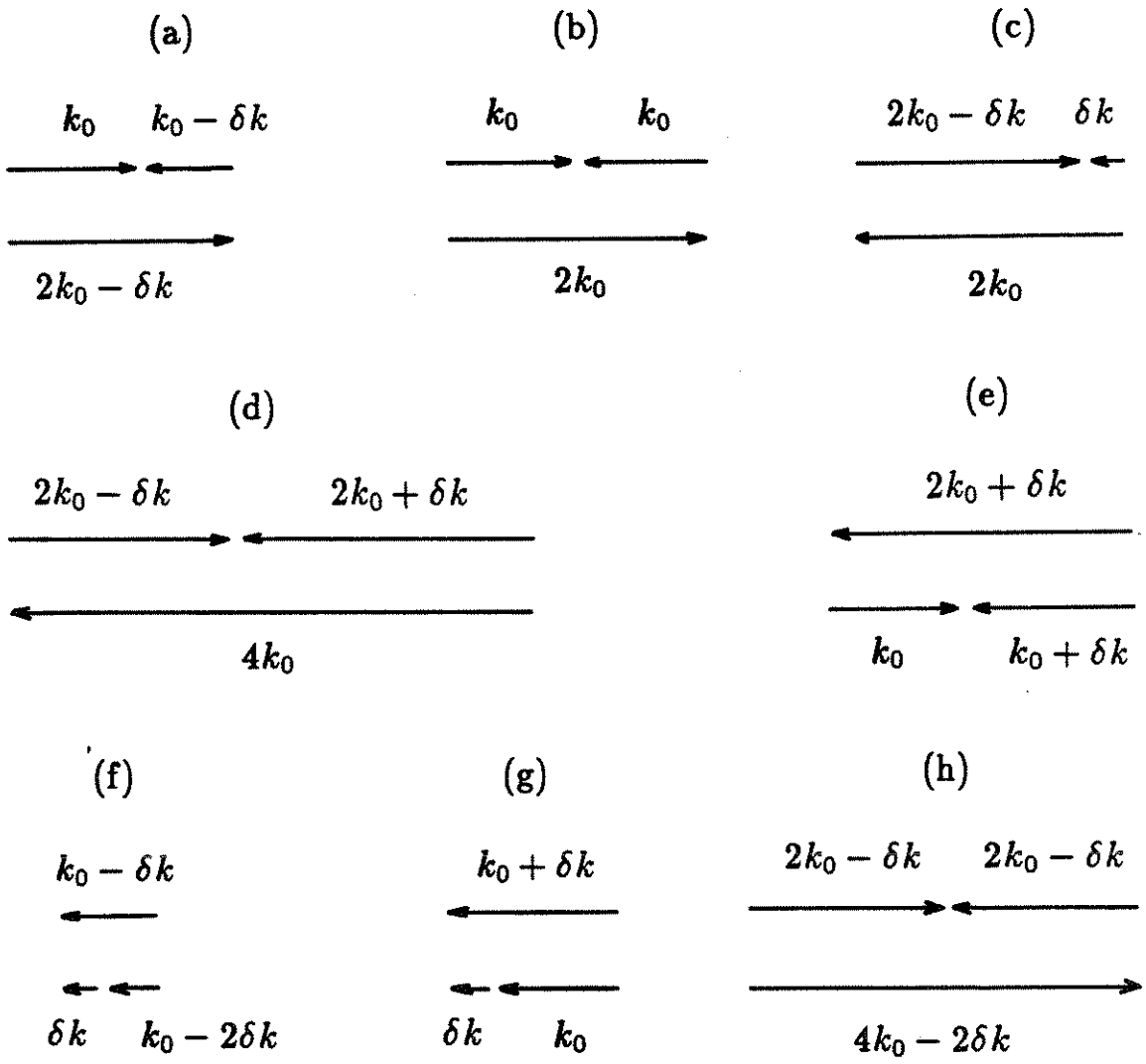

Figure 11: Wave-number–matching diagram showing: (a) SRS. (b) SBS. (c) The $k = -\delta k$ coupled mode. (d) The $k = -(2k_0 + \delta k)$ coupled mode. (e) Thomson scattering of the pump. (f) The second Stokes satellite. (g) Thomson scattering of the SBS reflected light. (h) Electron decay.

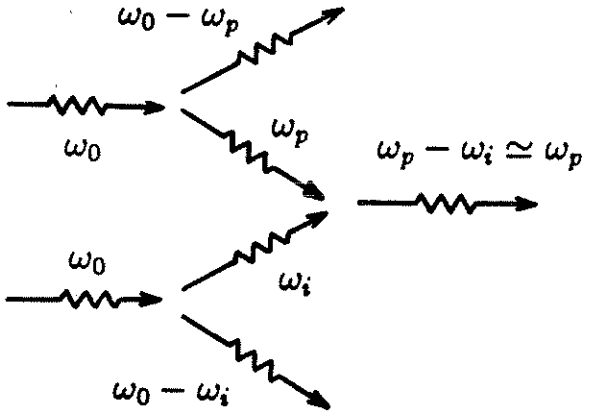

Figure 12: Schematic diagram showing the process of mode coupling between the SRS induced electron wave with the SBS induced ion wave to generate another electron wave.

diagram for this process is shown in Fig. 11(e). The ruby laser may also Thomson scatter from this same coupled mode and result in a light wave that is red shifted by ω_p. The SRS reflected light ($k = -[k_0 - \delta k]$) may Thomson scatter from the high phase velocity wave, the $k = -\delta k$ mode, and result in a light wave ($k = -[k_0 - 2\delta k]$), propagating in the backscattered direction, that is red shifted by $2\omega_p$, a second Stokes satellite. The k-matching diagram for this process is shown in Fig. 11(f). The second Stokes satellite may also scatter from the high phase velocity light wave and so on; in this way the backscattered light cascades to lower frequencies.

4.2 Observed Backscattered Spectrum

4.2.1 Experimental Results

The oscilloscope trace shown in Fig. 13(a) shows the expected red shifted satellite on the right, $\lambda = 11.1$ μm and the pump sideband blue shifted by the same amount, ω_p, on the left, $\lambda = 10.1$ μm. The unshifted SBS line does not appear in Fig. 13(a) because it was absorbed with an absorber (SF_6) in order to prevent saturation of the detector. The two signals in Fig. 13(a) were attenuated by different amounts and so the ratio of their amplitudes in Fig. 13(a) does not reflect the actual ratio. The actual amplitude of the blue shifted satellite was always less than that of the red shifted satellite.

4.2.2 Simulation Results

The experimental result mentioned in Sec. 4.2.1 was corroborated when a symmetrically shifted blue shifted (anti-Stokes) satellite was also detected in the backscattered spectrum in a computer simulation that closely modeled the experiment. The particle code that was used, WAVE [35], is a fully relativistic electromagnetic PIC code. The same value, $k_p\lambda_D = 0.2$, was used in both the simulation and the experiment. However, a value for the square root of the ion to electron mass ratio, $(M/m)^{1/2} = 100$ instead of $(M/m)^{1/2} = 43$, a value $\omega_0/\omega_p = 3$ instead of $\omega_0/\omega_p = 22$ and a value $v_0/c = 0.1$ instead of $v_0/c = 0.02$ was used in order to perform the simulation. The pump light was incident along the x direction and was polarized along y. Fig. 13(b) shows the backscattered light ω spectrum $(E_{\text{long.}}(\omega))^2$, including: the SBS signal at ω_0, the first Stokes line due to SRS that was red shifted by ω_p about the SBS backscattered line, and, in addition,

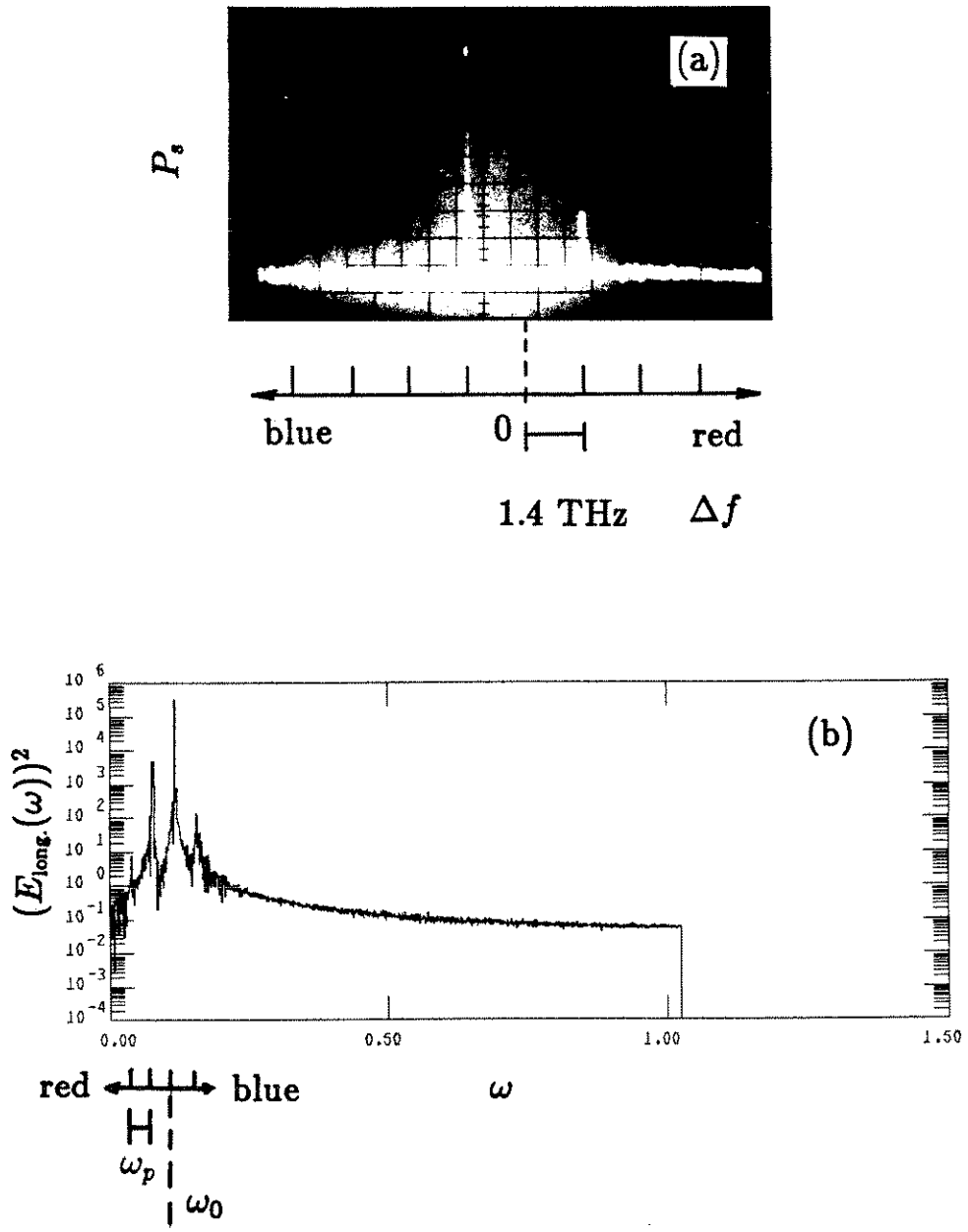

Figure 13: Infrared backscattered frequency spectrum from: (a) the experimental data and (b) a computer simulation that models the experiment.

two other lines that were due to higher order processes, a line symmetrically blue shifted about the SBS line and a second Stokes line that was red shifted by $2\omega_p$. The second Stokes line was not observed in the experiment. The acoustic shift, ω_i, could not be resolved in Fig. 13(b). Fig. 13(b) represents the ω spectrum at a time when SRS and SBS were occurring simultaneously. Up to 100% of the incident light was seen to be Brillouin-backscattered in this simulation.

In order to investigate mode coupling in a more controlled manner, another simulation was performed with a fixed amplitude ion ripple ($\tilde{n}_1/n_0 = 20\%$) and immobile ions. In this simulation, SBS could not occur and the ripple amplitude was a constant. Several differences between these results and those of the previous simulation were observed. As shown in Fig. 14(a), which is the same as Fig. 13(b) except with a constant ion ripple, the SRS was reduced considerably and the second Stokes satellite was not observed. However, the blue shifted satellite was again seen in the backscattered spectrum and its amplitude was approximately equal to the amplitude of the SRS. As shown in Fig. 14(b)—which shows n^2 vs. k—the slow counterpropagating wave, the $k = -(2k_0 + \delta k)$ mode, had an amplitude that approximately equaled the amplitude of the slow copropagating mode that would be due to SRS alone, the $k = 2k_0 - \delta k$ mode.

4.3 Observed Ruby Probe Spectrum

Three narrow frequency lines were observed when the collection lens for the ruby Thomson-scattered light was at $\theta_s = 7°$, the angle corresponding to $k = 2k_0(1 \pm 15\%)$; the uncertainty was due to the 4.5° angle subtended by the collection lens. The peak in the center of Fig. 15, which shows a photograph of the

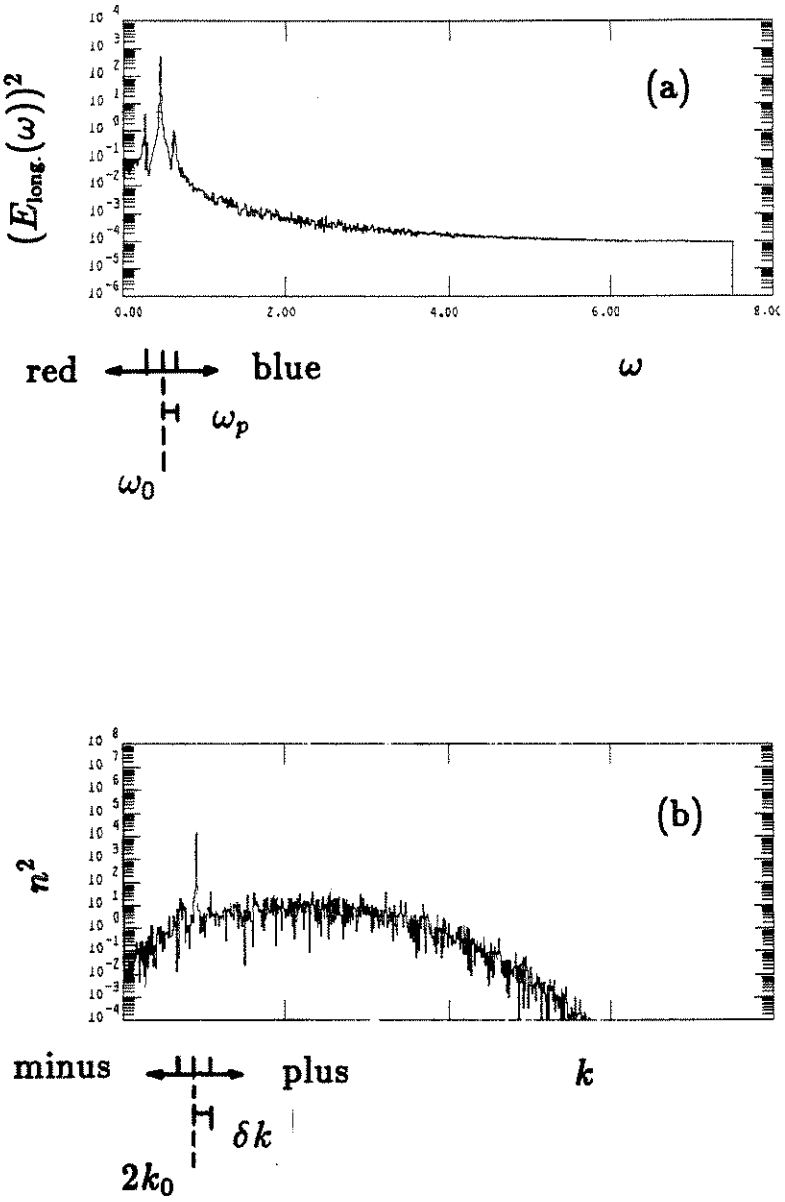

Figure 14: (a) Backscattered spectrum from a simulation with a constant ion ripple (20%) and immobile ions. (b) n^2 vs. k simultaneously with (a).

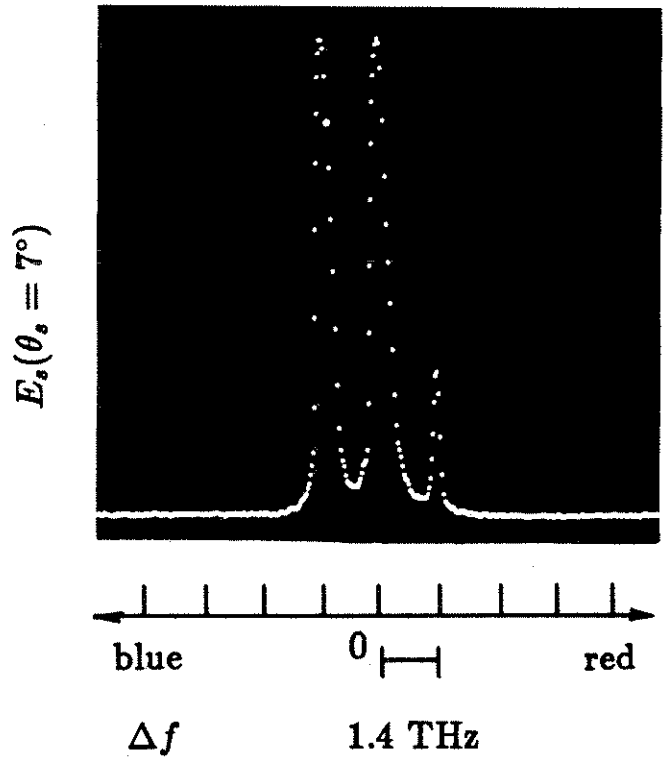

Figure 15: Ruby probe light Thomson-scattered from both a copropagating electron plasma wave (left), an ion wave (center) and a counterpropagating electron plasma wave (right).

optical multichannel analyzer output, is due to Thomson scattering from an SBS induced ion wave. SBS was expected because the pump laser intensity, I, was well above its threshold. This feature was detected only when the CO_2 laser was incident on the plasma and thus was not due to ruby stray light from specular reflections. The Thomson-scattered signal from the ion wave appears unshifted in frequency because the ion-acoustic frequency, ω_i, was less than the resolution of the spectrometer. The acoustic frequency was, nevertheless, measured by using

a spectrometer with a greater resolution and in this way the electron temperature was determined to be $T_e \simeq 10$ eV. The peak on the left of Fig. 15 is due to Thomson-scattered light that is blue shifted in frequency (Δf) by an amount that, assuming $\Delta\omega = \omega_0$ and $T_e = 10$ eV, is consistent with a plasma density of 2.0×10^{16} cm^{-3} ($n_0/n_c = 2 \times 10^{-3}$) and a value $k_0\lambda_D = 0.2$. Again, no peak was observed when the probe was fired without the CO_2 laser. These results imply that this was not incoherent scattering from thermal fluctuations, but collective scattering ($k\lambda_D \ll 1$) from the fundamental component of a plasma wave that was propagating in the direction of the pump with $(\omega, k) = (\omega_p, 2k_0 - \delta k)$. By varying the arc fill pressure and the relative timing between the preionization and the laser pulse, the plasma density could be continuously adjusted. The densities calculated from the frequency shifts of both the red shifted SRS and blue shifted peak of the 7° Thomson scattering agree over the density range of the experiment.

The red shifted satellite in the ($\theta = 7°$) ruby Thomson-scattered spectrum is the signature of a plasma wave with $\omega = \omega_p$ and $k = -(2k_0 + \delta k)$, counterpropagating with respect to the pump. The red shifted satellite was detected only in the presence of the blue shifted line. The amplitudes shown in Fig. 15 do not represent the actual relative amplitudes because each was attenuated by a different amount. When the actual attenuation factors were taken into consideration, the ratio of the amplitude of the counterpropagating wave to the copropagating wave in Fig. 15 was calculated to be approximately 4%. As shown in Fig. 16, the amplitude of the red shifted feature of the ruby Thomson-scattered spectrum was correlated with the product of the amplitudes of the blue shifted satellite and the line due to scattering from the ion wave.

The probe satellite has been observed previously [17], but we believe the blue

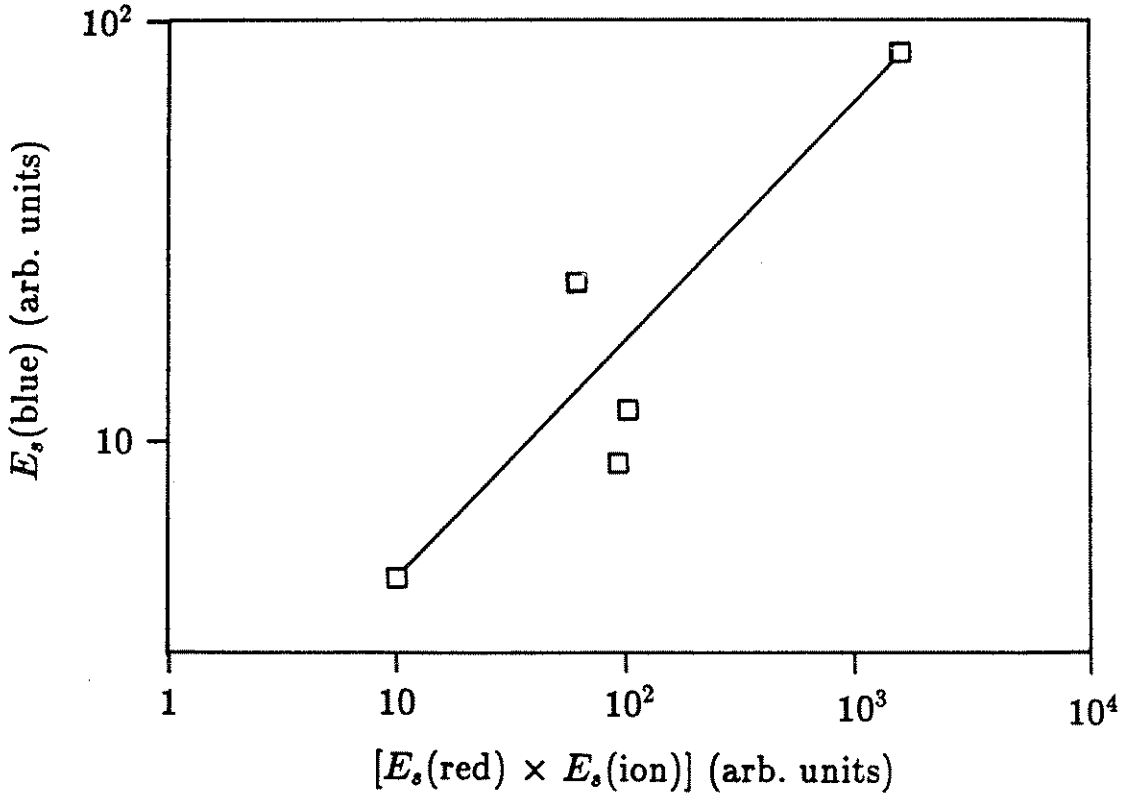

Figure 16: Correlation of the amplitude of the red shifted satellite of the ($\theta_s = 7°$) ruby Thomson-scattered spectrum with the product of the amplitude of the ion feature and the amplitude of the blue shifted satellite.

shifted pump satellite to be a new result.

4.4 Comparison with Theory

4.4.1 Backscattered Spectrum

The Blue Shifted Backscattered Satellite

As was mentioned in Sec. 4.1, the incident CO_2 pump light wave may Thomson scatter from the counterpropagating slow wave, the $k = -(2k_0 + \delta k)$ mode, and result in a backscattered light wave that is blue shifted by ω_p. The red shifted satellite is due to Raman scattering from the copropagating slow wave. It may be seen from the Bragg formula, Eq. 44 of Sec. 3.4, which applies to both Thomson scattering and SRS in the limit of $\tilde{n}_1/n_0 \ll 1$, that both depend on $(\tilde{n}_1/n_0)^2$. Therefore, the amplitude ratio of the blue to the red shifted backscattered satellite should approximately equal the square of the amplitude ratio of the perturbed densities of the counterpropagating to the copropagating slow waves. Comparing Fig. 14(a) with Fig. 14(b), we see that this was found to be the case in the simulation with a constant ion ripple.

It is predicted [12] that the ratio of the perturbed density of the counterpropagating to the copropagating slow wave should be approximately unity for a ripple of 20%. From the relative growth rates of the various predicted modes [12], only the fastest growing mode need be considered, their ω_1 mode [see their Fig. 1(b), using $q = (\epsilon/6)(c^2/v_e^2)(n/n_c) = 3.4$ where ϵ is the ion ripple density amplitude normalized to the background density and the other variables are as defined previously]. This was also found to be the case in the simulation, as shown

in Fig. 14(b), where the ripple amplitude was 20%. They also predict that the the ratio of the perturbed density of the high phase velocity mode to the copropagating slow mode should be $\ll 1$. This was found to be true in the simulation as well; it is in the noise in Fig. 14(b).

As was shown in Fig. 11(g), there is another way in which the blue shifted satellite may arise. The SBS reflected light ($k \simeq -k_0$), may Thomson scatter from the high phase velocity, mode coupled wave, the $k = -\delta k$ mode, and result in a light wave propagating in the backscattered direction ($k = -[k_0 + \delta k]$) that is blue shifted by ω_p. This contribution to the blue shifted satellite should be less than the contribution due to the pump Thomson scattering, that was shown in Fig. 11(e), by the product of SBS reflectivity and the square of the ratio of the density perturbation of the fast to the slow counterpropagating waves, $[(\tilde{n}_1/n_0)_{\rm fast}/(\tilde{n}_1/n_0)_{\rm slow}]^2 \simeq [(k_{\rm fast}/k_{\rm slow})(E_{\rm fast}/E_{\rm slow})]^2$. For an ion ripple of amplitude from $3 - 18\%$, as in our experiment, it is predicted [12] that, using $q = (\epsilon/6)(c^2/v_e^2)(n/n_c) = 0.5 - 3.0$, $E_{\rm fast}/E_{\rm slow}$ varies from unity by less than 50% [see their Fig. 3]. Thus $[(\tilde{n}_1/n_0)_{\rm fast}/(\tilde{n}_1/n_0)_{\rm slow}]^2 \sim 10^{-4} - 10^{-3}$, since $(k_{\rm fast}/k_{\rm slow}) \sim 0.02$. Again for this range of values for q, only the fastest growing mode, their ω_1 mode, need be considered [see their Fig. 1(b)]. And since the SBS reflectivity was $\leq 10\%$, the Thomson scattering of the SBS reflected light should be less than the Thomson scattering of the pump by a factor of $10^{-5} - 10^{-4}$. Thomson scattering of the SBS reflected light may therefore be neglected compared to Thomson scattering of the pump.

The Red Shifted Backscattered Satellite

The prediction that the growth rate of SRS is reduced by the ion ripple appears to be verified by the two simulation results. It was mentioned that the level of SRS was reduced in the simulation in which a fixed ion ripple was used from the level of SRS in the simulation in which the ion ripple was due to SBS. The fixed ion ripple was imposed before the SRS could begin to grow and so we would expect from theory [12] that the SRS would have a reduced growth rate.

The Second Stokes Backscattered Satellite

As was discussed in Sec. 4.1, the SRS reflected light could cascade further in frequency by coupling to the high phase velocity mode excited by mode coupling. [see Fig. 11(f)]. This would give rise to the second Stokes satellite in Fig. 13(b). We think that the reason that the second Stokes satellite was observed in the simulation without a fixed ion ripple but was not in the simulation with a fixed ion ripple was because the SRS was considerably greater in the former than in the latter.

4.4.2 Ruby Spectrum

The amplitude ratio of the blue shifted satellite to the red shifted satellite in the backscattered spectrum should also equal the amplitude ratio of the red shifted to the blue shifted satellite in the ruby Thomson scattered spectrum. When the proper attenuation factors in the experiment were taken into consideration, this was found to be the case.

Theory [12] predicts that for an ion ripple of $3\% - 10\%$ as in our experiment, the

low phase velocity, counterpropagating wave could have an amplitude that may be $2\% - 10\%$ of the amplitude of the slow copropagating wave. This is consistent with the amplitude of the low phase velocity, counterpropagating wave relative to the copropagating wave that was measured by ruby Thomson scattering, 4%.

Theory also [12] predicts that the amplitude of the slow counterpropagating mode ($k = -[2k_0 + \delta k]$), ie. the red ruby probe satellite, should be proportional to the amplitude of the slow copropagating mode ($k = 2k_0 - \delta k$), ie. the blue ruby probe satellite, with the constant of proportionality increasing with the size of the ion ripple, ie. the ion satellite. This prediction is in reasonable agreement with the results of Fig. 16, although the number of data points are limited.

Neither the mode which would arise from the plus sign nor any of the modes with other values of m were observed in the present experiment. This could be because spatial harmonics with greater values of k are more heavily Landau damped since $v_e/v_\phi = (m+1)k_2\lambda_D \simeq (m+1)(.2)$ and we never observed plasma waves when the plasma density was less by a factor of four, or $v_e/v_\phi \simeq .4$. Other authors also predict that the larger-k modes would be lower in amplitude. Specifically, the waves with k equal to $k = \pm 4k_0$ are predicted [12] to have amplitudes that are 20% of the amplitudes of the waves with $k = \pm 2k_0$. We would therefore not expect to see the $k \geq 4k_0$ modes since their amplitudes would have been beneath the detection threshold in the experiment.

4.4.3 Alternative Mechanisms

There are several mechanisms that could also possibly give rise to either a fast wave or a counterpropagating slow wave but none of them except quasi-resonant mode coupling can give rise to both with the correct wave numbers to be matched

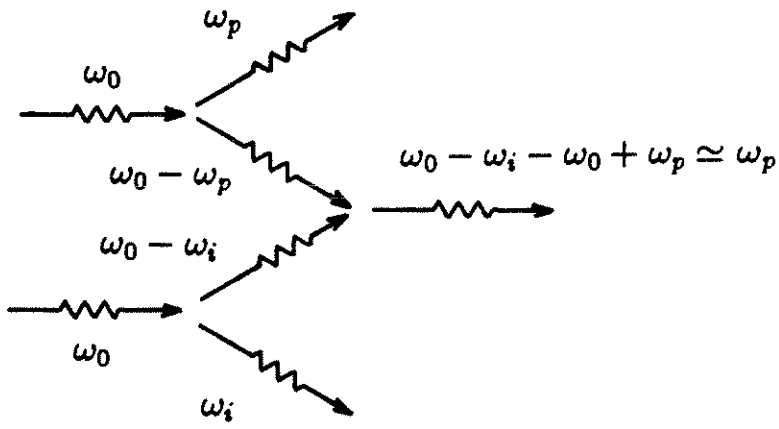

Figure 17: Schematic diagram showing the process of collinear optical mixing between the SRS reflected light wave and the SBS reflected light to excite the high phase velocity electron wave.

with the pump and the ruby probe. We include a discussion of each of them for completeness.

Collinear Optical Mixing

A high phase velocity electron wave $[(\omega, k) = (\omega_p, k_0 - k_1) = (\omega_p, -\delta k)]$ may also arise from the collinear optical mixing of the SRS reflected light $(k = -[k_0 - \delta k])$ with the SBS reflected light $(k = -k_0)$ The SBS reflected light is properly k-matched to Thomson scatter from the resulting fast wave and produce a backscattered wave $(k = -[k_0 + \delta k])$ that is blue shifted by ω_p. This process is shown diagramatically in Fig. 17. The corresponding k-matching diagram is shown in Fig. 11(g).

Optical mixing is similar to SRS except that instead of just one pump, two pumps, whose frequency difference is equal to the Bohm-Gross frequency, are

incident on the plasma. The wave grows not exponentially as an instability but linearly as a forced harmonic oscillator. The amplitude of the beat wave driven by optical mixing is given by [23],

$$A(t) = A(0) + \frac{1}{4}\alpha_0\alpha_1\left(\frac{\omega_p}{k_2}\right)\frac{\omega_0+\omega_1}{\omega_1}t = A(0) + \left(\frac{\gamma}{k_2}\right)t, \tag{46}$$

where,

$$\alpha_0 = \frac{eE_0}{mc\omega_0} = \frac{v_0}{c}, \qquad \alpha_1 = \frac{eE_1}{mc\omega_1}. \tag{47}$$

The factor $(\omega_0+\omega_1)/\omega_1$ is included only in the case of counterpropagating pumps. The saturated amplitude due to relativistic detuning is given by [23]

$$Ak = \left[\frac{16}{3}\left(\frac{c}{v_\phi}\right)^2\alpha_0\alpha_1\right]^{1/3} \tag{48}$$

We find that for the case of a high phase velocity beat wave, resulting from collinear optical mixing of an SRS reflected light wave (using a reflection coefficient of 0.2%) and an SBS reflected light wave (using a reflection coefficient of 10%), the predicted saturated amplitude of the beat wave from Eq. 48, using $v_0/c = 0.02$, is 1%. The time to saturation is $t \simeq 60$ ns $>> \tau$, where τ is the CO_2 laser pulselength. We therefore use Eq. 48 to find the maximum value for kA, $kA_{\max} \simeq 0.02\%$. It is predicted [12] that for these same experimental parameters, in which the amplitude of the copropagating slow wave is $\leq 10\%$, the maximum amplitude of the fast wave resulting from mode coupling should be $\tilde{n}_1/n_0 \leq .4\%$. Therefore, optical mixing is less effective than mode coupling in the regime of our experiment in exciting the fast wave.

Reflection from the Critical Layer

A counterpropagating slow wave would result from the reflection of the copropagating slow wave from its critical layer. This, however, is unlikely for several

reasons. First, the simulation was performed with a homogeneous plasma, which of course has no critical layer. In a quasi-homogeneous plasma, such as in a real experiment, the plasma wave would have difficulty reaching its critical layer to be reflected. Using the Bohm-Gross dispersion relation to find k_2 in terms of ω_p, and given $k_2\lambda_D = 0.2$ and a fixed temperature, we find that for the plasma wave to reach its critical density it would have to propagate to where the density changed by 12%. This would mean that it would have to propagate 2.4 cm if we assume a linear profile ($L = [(1/n_0)(dn/dx)]^{-1}$). If it begins near the top of a parabolic profile, it may not even have a critical layer. Experimentally, we found that the interaction region was located only 2 mm from the best focus of the CO_2 laser best focus, which was also probably the location of the peak density. And since it was at most 2 mm in length, it could not reach its critical layer to be reflected even if it had one.

SRS from an SBS Reflected Light Wave

The incident pump wave that is reflected from the ion mode in SBS may itself Raman scatter and decay into a plasma wave and another light wave. The plasma wave that is generated would be counterpropagating with respect to the initial incident pump wave and have almost the same frequency and wave number as the copropagating plasma wave. Since the SBS reflected light wave is shifted by ω_i, the frequency of the counterpropagating wave would differ from the co-propagating wave by the same amount. Even only a slight change in density, $\Delta n_0/n_0 \simeq (\omega_i/\omega_p)^2 \simeq (k\lambda_D)^2(m/M) \simeq 2 \times 10^{-5}$, would allow the instability to be resonant. The mismatch, therefore, is not a factor.

However, the reflected light would of course have to be above the SRS threshold

for this process to occur. The maximum incident pump intensity was measured to be only four times above the SRS threshold. Although it was not measured on the shots when the counterpropagating satellite was observed, the largest measured SBS reflection coefficient was found to be 10%. It is therefore unlikely that the SBS reflected light was also above the SRS threshold.

Electron Decay

It is well known that an electron plasma wave may decay into a copropagating ion wave and another counterpropagating electron plasma wave by a parametric decay instability in which a electron wave acts as the pump [36]. This is just like SBS, but instead of an electromagnetic, transverse wave reflecting from an ion mode, an electrostatic, longitudinal wave is reflected from an ion wave. The nonlinear coupling term in the force equation is now $(\mathbf{v}\cdot\nabla)\mathbf{v}$ instead of $(-e/m)(\mathbf{v}\times\mathbf{B})$. It can be shown that the same ponderomotive force term driving the ion wave results in both cases [37]. The process begins when the initial electron plasma wave is reflected from plasma noise. The ponderomotive force due to superposition of the fields of the two electron plasma waves, the reflected and initial wave, then beat together to generate an ion wave. The initial electron plasma wave is then further reflected and so both the ion wave and the reflected electron plasma wave grow exponentially.

The initial electron plasma wave (ω_2, k_2), the daughter ion wave (ω_3, k_3) and the beat electron plasma wave (ω_4, k_4) must obey their dispersion relations,

$$\omega_{2,4} = \omega_p(1 + 3(k_{2,4}\lambda_D)^2)^{1/2}, \qquad \omega_3 = k_3 c_s, \tag{49}$$

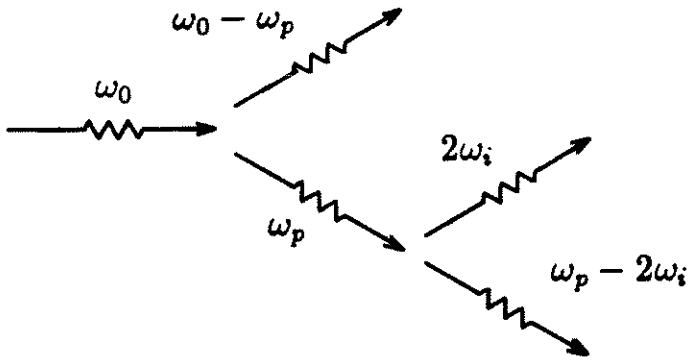

Figure 18: Schematic diagram showing the process of electron decay of an SRS induced electron plasma wave (ω_p) into an ion wave ($2\omega_i$) and another electron plasma wave ($\omega_p - 2\omega_i$).

and the phase-matching conditions,

$$\omega_2 = \omega_3 + \omega_4, \qquad \mathbf{k}_2 = \mathbf{k}_3 + \mathbf{k}_4. \tag{50}$$

If $\omega_3 \ll \omega_2$, then these conditions require that $(\omega_4, k_4) \simeq (\omega_2, -k_2)$ and that $k_3 \simeq 2k_2$. The process is shown diagramatically in Fig. 18. The corresponding wave-number–matching diagram is shown in Fig. 11(h). The resonant instability may occur when k_2 is greater than the critical value, $[(m/M)^{1/2}/\gamma]k_D$, where m/M is the electron to ion mass ratio and γ is the ratio of the specific heats. This condition is met for our experimental parameters. If this condition is met and if damping is neglected, the threshold for the instability is shown [36] to vanish in the collisionless limit.

The growth rate for electron decay is given by [36]

$$\frac{\omega}{k} = \left[\frac{\Lambda}{4k_0}\left(\frac{M}{m}\right)^{1/2}\right]^{1/3}, \tag{51}$$

where $\Lambda = {v_0}^2 m/T_e$ and ${v_0}^2 = (eE/m\omega_0)^2$. For our experimental parameters, the growth rate is small compared to the laser pulselength, $\omega\tau \sim 10^{-4}$. We would therefore not expect electron decay to occur.

The characteristic ion wave with $k_3 \sim 2k_2$ was not observed in the simulation. It could not be distinguished with ruby Thomson scattering from the ion wave second harmonic in the experiment.

As will be discussed in the next section, the counterpropagating slow wave produced by electron decay, even if it did occur, could not match to the pump or the probe to result in the blue shifted backscattered satellite or the red shifted ruby satellite.

Driven Electron Decay

The ion wave in the electron decay instability has almost the same frequency, wave number and direction as the second harmonic of an ion wave excited by SBS. Thus, if an electron plasma wave and a copropagating ion wave are both simultaneously present in the plasma, they may couple to excite a counterpropagating plasma wave. Since the beat plasma mode is an eigenmode of the plasma, it may grow to large amplitude. Again the phase-matching and dispersion relations for the electron decay instability must be satisfied. Unlike the case of electron decay, in the driven process, the electron plasma wave grows not exponentially, but linearly in proportion to the product of the amplitudes of the initial two pumps, the ion wave and electron plasma wave. Again the process is shown in Figs. 18 and 11(h).

The Raman-driven electron plasma wave ($k = 2k_0 - \delta k$) and the SBS-driven second harmonic ($k = 4k_0$) are not simultaneously ω- and k-matched to the counterpropagating mode that would result from the decay of the Raman-driven electron plasma wave ($k \simeq -[2k_0 - \delta k]$). The k-mismatch is $\Delta k/k \simeq (n/n_c)^{1/2} = 4\%$ for the experiment and 60% for the simulation. The frequency-mismatch, however, is only $\Delta\omega/\omega = (k\lambda_D)^2(\Delta k/k) = 0.2\%$ for the experiment and 2% for the

simulation since a factor of $\omega_p/\omega_0 \simeq 0.3$ was used.

Even if they did occur, the slow counterpropagating waves that would arise from any of these alternative mechanisms are not k-matched to either the pump and the blue shifted backscattered satellite or the ruby probe and the red shifted ruby satellite. This is because as was shown in Fig. 11(e), in order for a slow plasma wave to k-match to the pump and the light wave blue shifted by ω_p, it would have to have wave number, $k \simeq -(2k_0 + \delta k)$, which is just the wave number of the slow counterpropagating wave resulting from quasi-resonant mode coupling. A similar argument may be applied to ruby Thomson scattering. The counterpropagating wave that would be generated by any of these other mechanisms, on the other hand, would have $k \simeq -(2k_0 - \delta k)$. So of the mechanisms that could drive slow counterpropagating waves, only quasi-resonant mode coupling may explain the observed ruby and CO_2 Thomson scattered spectra.

4.5 Conclusion

If they occur simultaneously, the daughter electrostatic plasma waves that result from SRS and SBS may couple by quasi-resonant mode coupling to generate both slow and fast counterpropagating electron waves. The pump and the ruby probe light waves may then couple to the slow counterpropagating electron wave, whose frequency equals that of the original SRS induced electron wave, to generate new light waves that are Doppler-shifted by the plasma wave frequency. The SRS backscattered light wave may cascade to even lower frequency by coupling to the fast wave. This scenario is the only one consistent with both the ruby Thomson-scattered and the backscattered spectra.

Specifically, the red shifted ruby probe satellite is the result of the probe Thomson scattering from the counterpropagating, low phase velocity, mode-coupled wave. The amplitude of this coupled mode, relative to the slow copropagating wave, measured by the ruby probe, agrees with the theoretical predictions [12]. The correlation of Fig. 16 indicates that the same holds true for different values of the ion ripple. The relative amplitudes of the ant-Stokes backscattered satellite and the Stokes backscattered satellite are consistent with the assumption that the anti-Stokes backscattered satellite arises from the pump Thomson scattering from the slow counterpropagating coupled mode. The simulation indicates that cascading to lower frequency may occur and that the growth rate of SRS is reduced by the ion ripple. The fast wave that may be excited by optical mixing is much smaller in amplitude than the fast wave that may be excited by mode coupling in the regime of the experiment. Finally, since the slow counterpropagating waves that were excited by any of the alternative mechanisms are not phase-matched to either the pump or the probe, only mode coupling may explain the observed scattered spectrum.

Chapter 5

Implications and Summary

5.1 Implications

5.1.1 Reduction of SRS Growth due to Nonlinearities

Reduction due to Steepening

Because of the conditions on phase-matching, the pump can only backscatter from the fundamental of the plasma wave. So the growth of higher harmonics drains pump photons which would otherwise have gone into reflected photons. Wave steepening may therefore reduce the growth of SRS.

SRS may also be reduced by steepening because the trapping of electrons [4], discussed in Sec. B, may be increased by the distortion of the waveform.

Reduction due to Mode Coupling

Just as in the case of pure harmonics, the pump cannot phase-match with the spatial harmonics. So the growth of spatial harmonics, either by mode coupling

may also reduce backscatter.

We have seen that since SRS light waves may match to the fast wave, this mode may redistribute the backscattered light into other frequency modes by cascading. This in turn reduces the amount of photon energy that goes into the copropagating wave, which in turn should reduce the backscatter. It has been predicted that cascading may significantly reduce the amplitude of the beat wave in studies of the beatwave accelerator [18] [19].

However, the presence of the ion wave fluctuation may have several other effects on SRS. For instance, the presence of ion wave fluctuations may actually lower the threshold for SRS [22]. Also, mode coupling is thought to explain the observed quenching of SRS in both experiments [38] and simulation [41]. Although in our experiments no detailed, simultaneous, time resolved measurements of SBS and SRS excited wave at different densities were carried out to study the interplay between the two instabilities, we observed that as the plasma density was increased from $(0.1\%)n_c$ to $(1\%)n_c$, SBS increased whereas SRS gradually diminished. In fact no SRS was ever observed for plasma densities greater that $(2\%)n_c$.

5.2 Summary

In summary, we have simultaneously observed the decay products of a light wave undergoing stimulated Raman scattering. We have used ruby Thomson scattering to detect the daughter plasma wave while simultaneously observing the backscattered daughter light wave. Also using ruby Thomson scattering, we have observed the harmonics of plasma waves driven by SRS and found their frequencies, wave

numbers, and amplitudes to be consistent with warm-plasma wave-steepening theory.

We also observed the usual decay products of SBS, the backscattered light wave and the ion wave, including its harmonics. Using ruby Thomson scattering, we have detected a counterpropagating electron plasma wave with approximately the same phase velocity as the copropagating electron plasma wave. In addition to the usual satellite red shifted by the plasma wave frequency in the backscattered spectrum, we have observed a blue shifted satellite. A computer simulation not only confirms this result but reveals a cascading of light towards lower frequency. All of these spectral features may be explained by Thomson scattering from both high and low phase velocity, counterpropagating electron plasma waves, which originated from quasi-resonant mode coupling of an SBS induced ion wave with an SRS induced electron wave. The red shifted line in the ruby spectrum and the blue shifted shifted satellite in the backscattered spectrum are the result of Thomson scattering from the low phase velocity wave. The second Stokes satellite is the result of the SRS reflected light coupling to the fast wave and further cascading to light waves with frequencies lower by the electron-plasma–wave frequency.

By siphoning energy into other modes, both wave steepening and mode coupling may reduce the Raman backscatter instability.

5.2.1 Future Experiments

Some interesting future experiments would include:

- Search for half harmonics of the electron plasma wave.
- Investigate the dependence of SRS sidescatter on angle.

- Study the interplay between SRS and SBS by time resolving both the electron plasma wave and the ion-acoustic wave simultaneously.
- Simultaneously streak the light Thomson-scattered from the counterpropagating electron plasma wave, the ion wave second harmonic and the copropagating electron plasma wave. Also, control the ion wave amplitude with a heavy ion. This would help to further discern whether resonant mode coupling or the electron decay instability is the dominant mechanism.
- Using $\alpha \ll 1$ ruby Thomson scattering, look for evidence of heating due to trapping.

Chapter 6

Appendix

Appendix A

CO_2 Laser System

A schematic of the CO_2 laser system is shown in Fig. 19. The acoustically modelocked oscillator generates a linearly polarized train of ($\tau = 1.5$ ns FWHM) pulses, separated in time by the cavity roundtrip time, 14 ns. The modelocking is accomplished by the periodic deflection of light with a period which equals the cavity transit time. The Bragg deflection is caused by acoustic oscillations that are excited in a Germanium crystal by an RF driven (30 MHz) pizoelectric transducer.

The pulse with maximum amplitude is selected using an electro-optic switchout. This operates on the basis of the Pockel's effect in which an electric field imposed on a Cadmium Telluride crystal rotates the polarization of passing light. The first light pulse triggers the breakdown of a spark gap that determines the starting time for an electric field that is generated by a DC power supply. The duration of the field is determined by a pulse forming cable. The time and duration are chosen such that crystal rotates the polarization of only the maximum amplitude pulse. A cross polarizer then passes the peak pulse and reflects the other pulses.

The transmitted pulse passes through a beam splitter which partially reflects

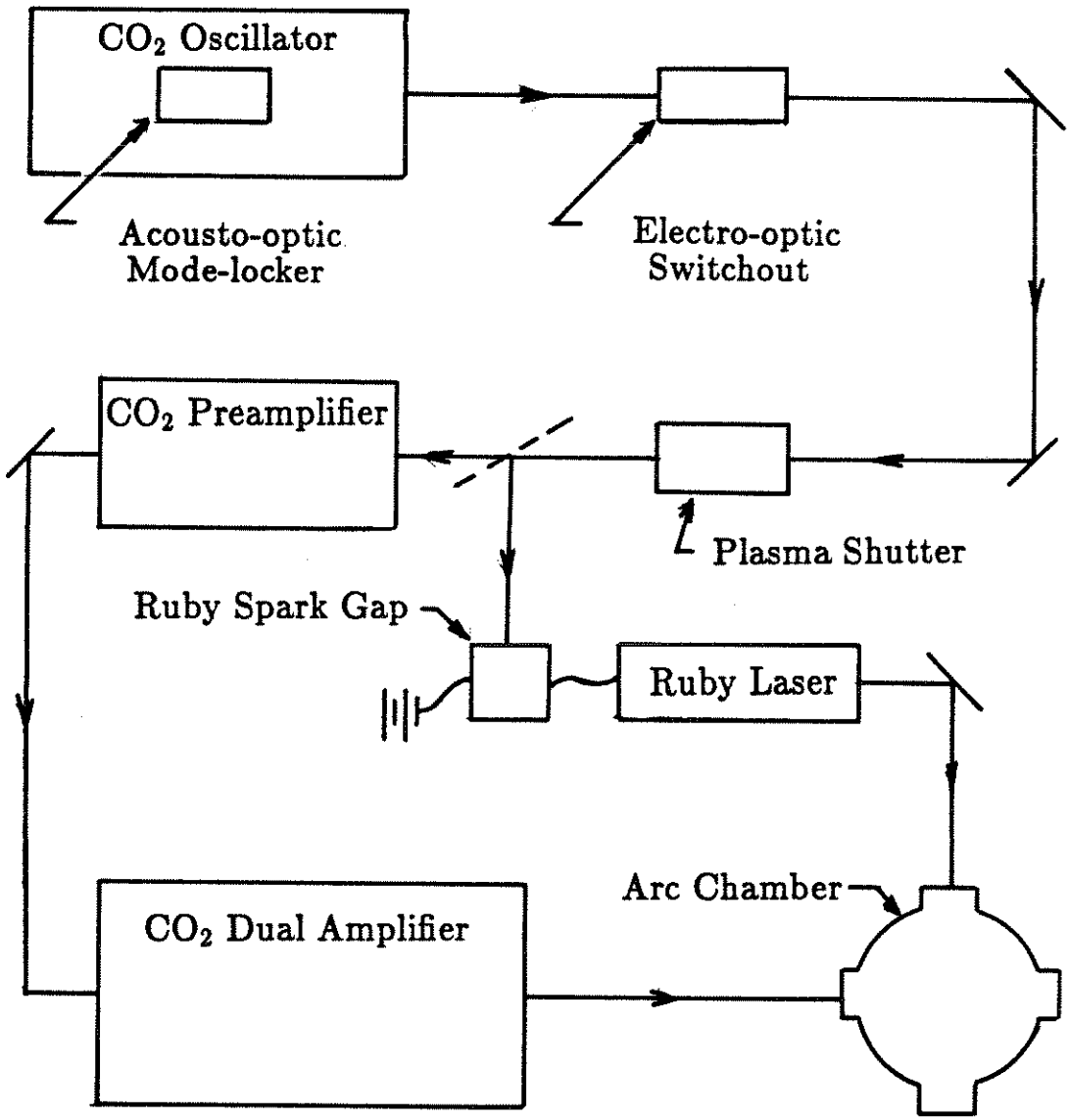

Figure 20: Schematic of the CO_2 laser system.

20% of it onto another spark gap. This spark gap triggers the Q switch of a ruby laser diagnostic beam so that the two pulses, the CO_2 and the ruby pulse, both arrive at the target simultaneously.

The single pulse then encounters a combination spatial filter, beam collimator and plasma shutter. This is comprised of a lens and concave mirror in a Keplerian telescope configuration. A metal pinhole, 1 mm dia., is placed at the focus of the beam. Spatial filtering results from elimination of the higher-order spatial modes, which have the greatest radius. Collimation of the beam may be accomplished by adjusting the separation between the lens and the mirror. Plasma shuttering results from the breakdown of air by the high intensity backscattered light. The light from the oscillator is below the breakdown threshold. Because it is defocused by the plasma that is created by the air breakdown, the amplified backscattered light, which normally retraces the rays of the incident light, is thus prevented from damaging the switchout and oscillator optics.

The 10 mJ pulse is then amplified by three transverse discharge amplifiers. It double passes the first amplifier. Then it is brought back and forth across the room in order to delay it optically. This is done because it needs to arrive at the target synchronously with the ruby diagnostic beam, which has a finite buildup time. Finally, it double passes a pair of large aperture amplifiers, after which it has a final energy of 5-10 J.

wavebreaking occurs in a cold plasma at $\tilde{n}_1/n_0 = 1$. As discussed in Sec. 2.3, it may occur in a warm plasma with our plasma temperature at $\tilde{n}_1/n_0 \sim 0.3$. Clearly, wave breaking would prevent the plasma-wave amplitude from ever reaching the maximum value that is predicted from finite pump amplitude considerations.

Above threshold and pump depletion, the plasma wave would grow until wavebreaking occurred. However, damping mechanisms may lead to saturation of the plasma wave and the SRS reflectivity before wavebreaking.

B.1 Anomalous Landau Damping

One possible damping mechanism is the nonlinear heating of trapped electrons. Electrons in the tail of the distribution may be accelerated to a temperature on the order of $T_e = (1/2)mv_\phi^2$. For the present experiment, this corresponds to $T_e = 0.25$ KeV. The consequent non-Maxwellian distribution leads to anomalous Landau damping. This effect is discussed in a paper on an SRS experiment [40] with parameters similar to our own. In that experiment, the saturated amplitude of the plasma wave was both predicted and measured to be $\tilde{n}_1/n_0 = 2\%$. Considering the results of Section 3.5, this mechanism is thus a candidate cause of the saturation of the plasma wave in the present experiment as well.

Bibliography

[1] D. Umstadter, R. Williams, C. Clayton and C. Joshi, Phys. Rev. Lett., **59**, 292 (1987).

[2] J. M. Dawson, Phys. Review **113**, 383 (1959).

[3] E. A. Jackson, Phys. Fluids **3**, 831 (1960).

[4] D. W. Forslund, J. M. Kindel, and E. L. Lindman, Phys. Fluids **18**, 1002 and 1017 (1975).

[5] P. Koch and J. Albritton, Phys. Rev. Lett. **34**, 1616 (1975).

[6] L. S. Kuz'menkov, A. A. Sokolov, and O. O. Trubachev, Izv. Vyssh. Uchebn. Zaved. Fiz. **12**, 17 (1983) [Sov. Phys. J. **26**, 1076 (1984)].

[7] J. Rosensweig, Phys. Rev. Lett. **58**, 555 (1987).

[8] J. P. Klozenberg, Phys. Fluids **14**, 94 (1971).

[9] G. McIntosh, H. Houtman, and J. Meyer, Phys. Rev. Lett. **57**, 337 (1986), and references quoted therein.

[10] W. L. Kruer et al. Phys. Fluids **23**, 1326 (1980).

[11] C. J. Walsh and H. A. Baldis, Phys. Rev. Lett. **48**, 1483 (1982); C. Clayton, C. Joshi and F. F. Chen, Phys. Rev. Lett. **51**, 1656 (1983).

[12] H. Barr and F. Chen, Phys. Fluids **30**, 1180 (1987).

[13] H. Figueroa and C. Joshi, Phys. Fluids, **30**, 2294 (1987).

[14] C. H. Aldrich, B. Bezzerides, P. F. Du Bois, and H. A. Rose, Comments Plasma Phys. Controlled Fusion **10**, 1 (1986).

[15] P. K. Kaw and J. Dawson, Phys. Fluids **16**, 1967 (1973).

[16] C. Darrow et al. Phys. Rev. Lett. **56**, 2629 (1986).

[17] D. M. Villeneuve, C. J. Walsh, and H. A. Baldis, Phys. Fluids **28**, 1591 (1985).

[18] S. H. Batha and C. J. McKinstrie, IEEE Trans. Plasma Sci., **PS-15**, 131 (1987).

[19] S. J. Karttunen and R. R. Salomaa, IEEE Trans. Plasma Sci., **PS-15**, 134 (1987).

[20] C. E. Clayton, C. Joshi, C. Darrow, and D. Umstadter, Phys. Rev. Lett. **54**, 2343 (1985).

[21] T. Kawabe, S. Kojima, and K. Takayama, J. Phys. Soc. Japan **20**, 1539 (1965).

[22] K. Estabrook and W. L. Kruer, Phys. Rev. Lett. **53**,465 (1984).

[23] M. N. Rosenbluth and C. S. Liu, Phys. Rev. Lett. **29**, 701 (1972).

[24] H. S. C. Wang, Phys. Fluids **6**, 1115 (1963).

[25] N. N. Bogolyubov and Y. A. Mitropolskii, *Asymptotic Methods of Nonlinear Oscillation Theory* [in Russian], Moscow, 42 (1974).

[26] T. P. Coffey, Phys. Fluids, **14**, 1402 (1971).

[27] H. A. Baldis, N. H. Burnett, and M. C. Richardson, Rev. Sci. Instrum. **48**, 173 (1977).

[28] J. Sheffield, *Plasma Scattering of Electromagnetic Radiation*, New York, 81 (1975).

[29] C. Liu, M. Rosenbluth, and R. White, Phys. Fluids **17**, 1219 (1974).

[30] R. G. Watt, R. D. Brooks and Z. A. Pietrzyk, Phys. Rev. Lett. **41**, 170 (1978).

[31] C. V. Raman and N. S. Nath, Proc. Ind. Acad. Sci. **2**, 406 and 413 (1935); 75, 119 and 459 (1936) [in five parts].

[32] C. Clayton, *The Physics of the Ion Acoustic Wave Driven by Stimulated Brillouin Scattering Instability*, thesis, UCLA (1983).

[33] R. E. Slusher and C. M. Surko, Phys. Fluids **23**, 472 (1980).

[34] W. L. Kruer, Phys. Fluids **23**, 1273 (1980).

[35] R. L. Morse and C. W. Neilson, Phys. Fluids **14**, 830 (1971).

[36] B. D. Fried, T. Ikemura, K. Nishikawa and G. Schmidt, Phys. Fluids **19**, 1975 (1976).

[37] G. Schmidt, *The Physics of High Temperature Plasmas*, New York, 47 (1979).

[38] C. J. Walsh, D. M. Villeneuve, and H. A. Baldis, Phys. Rev. Lett. **53**, 1445 (1984).

[39] R. Z. Sagdeev and A. A. Galeev, *Nonlinear Plasma Theory* (Benjamin, New York, 1969), p. 16.

[40] A. A. Offenberger, R. Fedosejevs, W. Tighe, and W. Rozmus, Phys. Rev. Lett. **49**, 371 (1982).

[41] G. Bonnaud, Laser and Part. Beams **5**, part 1, 101 (1987).